minerals

MDPI

Article

Trace Element Geochemistry of Sulfides from the Ashadze-2 Hydrothermal Field (12°58′ N, Mid-Atlantic Ridge): Influence of Host Rocks, Formation Conditions or Seawater?

Irina Melekestseva [1,*], Valery Maslennikov [1], Gennady Tret'yakov [1], Svetlana Maslennikova [1], Leonid Danyushevsky [2], Vasily Kotlyarov [1], Ross Large [2], Victor Beltenev [3] and Pavel Khvorov [1]

1 Institute of Mineralogy, South Urals Federal Research Center of Mineralogy and Geoecology UB RAS, Chelyabinsk District, 456317 Miass, Russia; maslennikov@mineralogy.ru (V.M.); genatret@yandex.ru (G.T.); svmas@mineralogy.ru (S.M.); kotlyarov@mineralogy.ru (V.K.); khvorov@mineralogy.ru (P.K.)

2 CODES ARC Centre of Excellence in Ore Deposits, University of Tasmania, 7001 Hobart, Australia; l.dan@utas.edu.au (L.D.); ross.large@utas.edu.au (R.L.)

3 VNIIOkeangeologiya, 190121 St. Petersburg, Russia; v.belt@yandex.ru

* Correspondence: melekestseva-irina@yandex.ru; Tel.: +7-9507447301

Received: 29 June 2020; Accepted: 17 August 2020; Published: 22 August 2020

Abstract: The trace element (TS) composition of isocubanite, chalcopyrite, pyrite, bornite, and covellite from oxidized Cu-rich massive sulfides of the Ashadze-2 hydrothermal field (12°58′ N, Mid-Atlantic Ridge) is studied using LA-ICP-MS. The understanding of TE behavior, which depends on the formation conditions and the mode of TE occurrence, in sulfides is important, since they are potential sources for byproduct TEs. Isocubanite has the highest Co contents). Chalcopyrite concentrates most Au. Bornite has the highest amounts of Se, Sn, and Te. Crystalline pyrite is a main carrier of Mn. Covellite after isocubanite is a host to the highest Sr, Ag, and Bi contents. Covellite after pyrite accumulates V, Ga and In. The isocubanite+chalcopyrite aggregates in altered gabrro contain the highest amounts of Ni, Zn, As, Mo, Cd, Sb (166 ppm), Tl, and Pb. The trace element geochemistry of sulfides is mainly controlled by local formation conditions. Submarine oxidation results in the formation of covellite and its enrichment in most trace elements relative to primary sulfides. This is a result of incorporation of seawater-derived elements and seawater-affected dissolution of accessory minerals (native gold, galena and clausthalite).

Keywords: Ashadze-2 hydrothermal field; copper sulfides; formation conditions; LA-ICP-MS; Mid-Atlantic Ridge; mode of occurrence; physico-chemical modeling; trace elements

1. Introduction

The understanding of the distribution and the mode of occurrence of trace elements (TEs) in sulfides is highly important, since these minerals are potential sources for byproduct TEs. Depending on the formation conditions and the mode of their occurrence, sulfide minerals exhibit specific TE associations [1–10]. The contents and the mode of occurrence of TEs, however, can dramatically change during the replacement of one sulfide by another, as was recently shown for primary and secondary sulfides of the Semenov-2 hydrothermal field, 13°30′ N, Mid-Atlantic Ridge (MAR) [11]. Thus, a potential sulfide concentrate would contain various Cu minerals (primary hydrothermal chalcopyrite and isocubanite and supergene minerals of the covellite group) with a different mode of occurrence of TEs [11,12].

The LA-ICP-MS-based analytical data on TE composition of seafloor sulfides are still strongly limited in comparison with continental minerals [3,8–18]. Due to variety of geodynamic settings,

host rocks and local formation conditions, seafloor sulfides are often characterized by diverse TE composition, indicating that a common model of TE behavior requires, at least, more TE data. Thus, analyzing seafloor sulfides with a LA-ICP-MS technique, we approach a better understanding of their formation conditions and TE distribution.

Here, we examine the trace element geochemistry of primary (isocubanite, chalcopyrite, pyrite) and secondary (bornite, covellite) sulfides from Cu-rich massive sulfide samples of the ultramafic-associated Ashadze-2 hydrothermal field, Atlantic Ocean. We will show (i) the potential use of elemental associations to predict the mode of TE occurrence; (ii) remarkable features of sulfides, which reflect their specific formation conditions; (iii) the change in the mode of TE occurrence during the replacement of primary minerals by secondary covellite; and (iv) the effective role of seawater and submarine oxidation in TE redistribution.

2. Geological Background

The Ashadze-2 hydrothermal field (12°99′ N, 44°91′ W; MAR) is part of the Ashadze hydrothermal cluster, which consists of four hydrothermal fields located between the Fifteen Twenty and Marathon fracture zones (Figure 1a). The Ashadze-1 hydrothermal field was discovered in 2003 by the Polar Marine Geosurvey Expedition (PMGE, St. Petersburg, Russia) [19,20]. The active Ashadze-2 hydrothermal field is located 4.3 km west of the Ashadze-1 field on the western wall of a rift valley, at a depth of 3100–3350 m (unpublished in-house report of PGME, 2007; [21]) and is associated with ultramafic and gabbroic rocks [19,20].

Black smokers of the Ashadze-2 field (at a depth of 3300 m) occur in a narrow (about 70 m) N–S trending graben-like trough bounded to the east by a faulted gabbroic body [22]. To the west, it is limited by a narrow N–S trending ridge, 20 to 50 m high, which bears numerous extinct hydrothermal chimneys. A high resolution (up to 30 cm) topographic survey in the Ashadze-2 field revealed a chain of hydrothermal mounds and a crater-shaped structure 20–25 m in diameter and 1–3 m deep [22,23]. Subsequent visual observations revealed black smokers on the crater bottom, indicating recent hydrothermal activity. The small active crater is interpreted as a submarine volcano built up with a mixture of carbonates and secondary copper sulfides and copper chlorides. A maximum temperature of 296 °C was measured for these fluids, but measurements were difficult, because the remotely operated vehicle could not be positioned adequately in the bottom of the crater [23]. The true temperature is therefore probably higher.

Massive sulfide chimneys are associated with the active smokers at the center of the crater [22,23]. Many inactive carbonate/sulfide mounds are also aligned along a N–S depression. Two types of hydrothermal deposits are observed: massive copper-rich sulfides associated with the black smokers and carbonate/sulfide chimneys. Average composition of the Ashadze-2 hydrothermal deposits is Fe 26%, Si 11%, Cu 11%, Zn 5%, Ca 8% [22]. Among non-sulfide minerals, aragonite is dominant, Mg-calcite is rare, and talc is common.

Five massive sulfide bodies were found within the Ashadze-2 hydrothermal field (Figure 1b) (unpublished in-house report of PMGE, 2007; [21]). The largest ore body (number I) is approximately 125 m by 335 m in size. Massive sulfide bodies in the south (numbers III and IV) are mostly composed of Fe-sulfides (pyrite and marcasite), whereas those in the center and far north (numbers I, II, and V) contain significant amounts of Cu and Zn sulfides (Figure 1b). The maximum age of sulfides from the Ashadze-2 hydrothermal is estimated at 27.3 ± 1.8 ky [21].

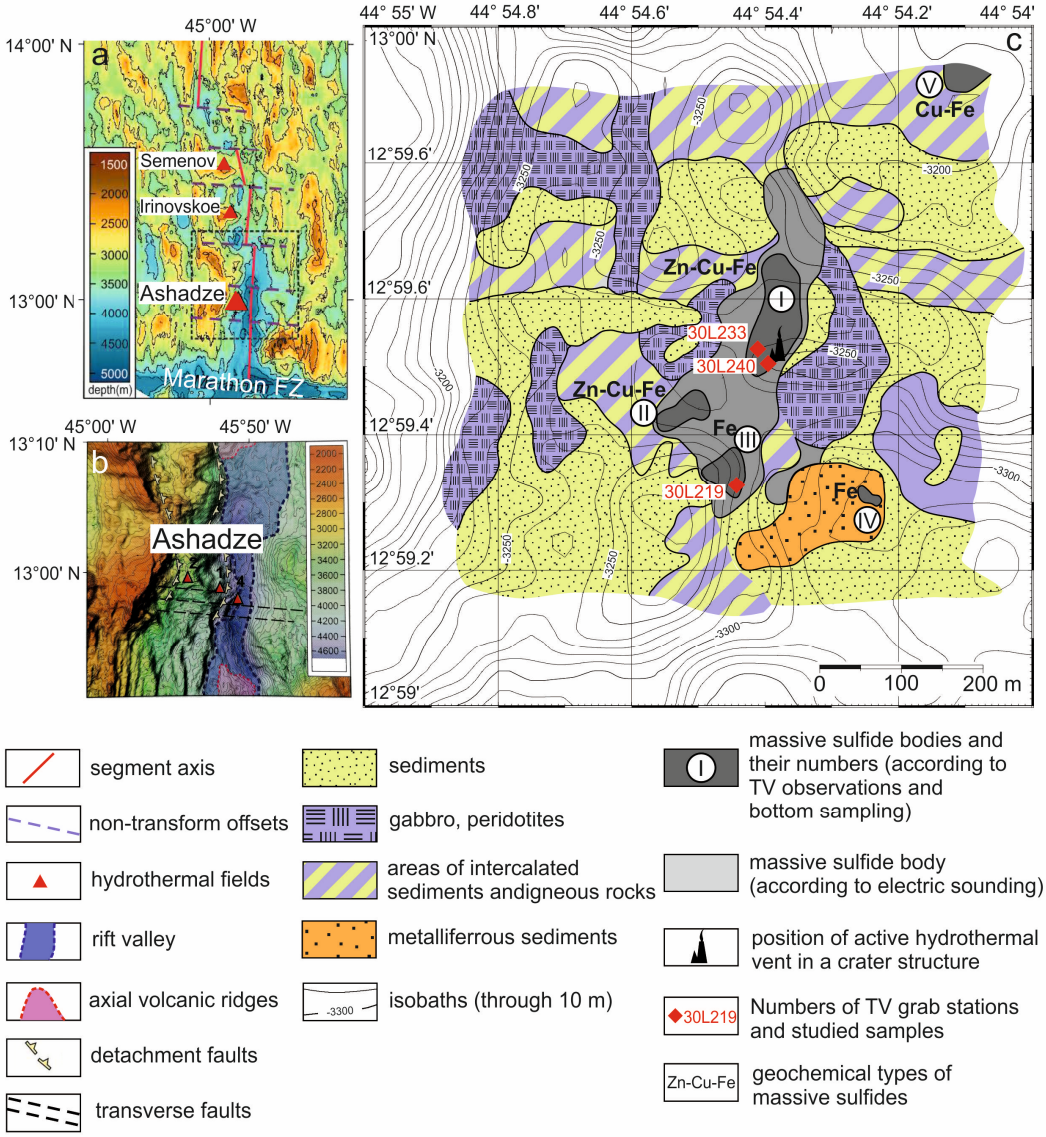

Figure 1. Location of the Ashadze hydrothermal cluster in the Mid-Atlantic Ridge (MAR); (**a**) modified after Figure 1 in [24], position of the Ashazde hydrothermal fields within the hydrothermal cluster; (**b**) modified from [25] and schematic structure of the Ashadze-2 hydrothermal field; (**c**) simplified after an unpublished in-house report by the Polar Marine Geosurvey Expedition (PMGE), 2007. TV—television grab station.

Debris around massive sulfide bodies includes numerous fragments of gossans, which consist of poorly lithified yellow, ochreous to reddish brown aggregates of Fe-oxyhydroxides [26]. They replace primary sulfides and sulfide clasts mixed with sepiolite clay and contain accessory pyrite, Cu–Fe sulfides (isocubanite and chalcopyrite), galena, atacamite, apatite, halite, Mn-hydroxides, uraninite, and an identified Th–Zr mineral.

3. Materials and Methods

Samples of massive sulfides from the Ashadze-2 hydrothermal field were collected in 2007 during the 30th cruise of the R/V Professor Logatchev using a TV grab at stations 30L219, 30L233, and 30L240 (hereafter, stations 219, 233, and 240, respectively) (Table 1). All TV grabs were positioned within the contours of massive sulfide bodies, distinguished according to electric sounding (Figure 1b).

Table 1. Coordinates of TV-grab sampling stations at the Ashadze-2 hydrothermal field, MAR (unpublished in-house report by the PMGE, 2007).

Station Number	Date	Time	Latitude	Longitude	Depth, m
219	May 27	19:32	12°59.322	44°54.443	3281
233	May 30	01:37	12°59.525	44°54.411	3266
240	May 31	13:55	12°59.504	44°54.395	3273

Stations 233 and 240 grabbed strongly oxidized sulfide material of ore body no. 1 close to an active hydrothermal vent (Figure 1b). Samples of station 233 (~30 kg) contained ~70% (hereinafter, the approximate percentage is taken from unpublished in-house report by PMGE (2007), according to on-board macroscopic description) of Fe-rich massive sulfides, ~30% of Fe–Mn oxyhydroxide and Fe–Si sediments, and single fragments of Cu-rich massive sulfides. Samples of station 240 (~300 kg) included 80% of Cu–Zn- and Fe-rich massive sulfides, ~20% of Fe–Mn oxyhydroxide and Fe–Si sediments, and a few pieces of black smoker chimneys. Station 219 (~60 kg) contained ~95% of altered gabbro and peridotites with stringer-disseminated sulfides and ~5% of Fe–Mn and Fe–Si crusts. According to the unpublished in-house report by PMGE (2007), the chemical composition of seafloor Cu-rich massive sulfides is highly variable (stations 233 and 240, respectively): 10.20–43.88 and 16.04–37.88 wt % Fe, 13.35–33.21 and 3.75–29.63 wt % Cu, 0.07–0.77 and 0.06–3.05 wt % Zn, 0.003–0.02 wt % Pb in both stations, 0.002–0.01 wt % Ni in both stations, 0.024–0.158 and 0.009–0.176 wt % Co, 5.03–10.08 and 0.19–10.34 ppm Au, 8.0–28.6 and 7.4–30.7 ppm Ag, and up to 289.5 ppm Sn (in one analysis). The Cu-rich samples were examined using an Axiolab (Carl Zeiss) optical microscope and a REMMA-202M SEM equipped with a Link ED-System at the South Urals Federal Research Center of Mineralogy and Geoecology UB RAS, Institute of Mineralogy, Miass (IMin), Russia. SEM studies were carried out using a 1-micron electron beam, 15 nA beam current, 20 kV accelerating voltage, and a counting time of 120 s for peak (standard MINM-25-53, ASTIMEX Scientific Limited, mineral mount No. 01-044). The mineral composition of massive sulfide samples was also refined on a SHIMADZU XRD-6000 diffractometer (Cu anode, graphite monochromator) at the IMin.

Quantitative LA-ICP-MS analysis of isocubanite, chalcopyrite, bornite, pyrite and covellite for major (^{57}Fe, ^{65}Cu) and trace elements (^{24}Mg, ^{27}Al, ^{29}Si, ^{43}Ca, ^{49}Ti, ^{51}V, ^{53}Cr, ^{55}Mn, ^{59}Co, ^{60}Ni, ^{66}Zn, ^{69}Ga, ^{75}As, ^{77}Se, ^{88}Sr, ^{95}Mo, ^{107}Ag, ^{111}Cd, ^{115}In, ^{117}Sn, ^{121}Sb, ^{125}Te, ^{137}Ba, ^{182}W, ^{197}Au, ^{205}Tl, ^{208}Pb, ^{209}Bi, ^{238}U) was carried out on a New Wave 213-nm solid-state laser microprobe coupled to an Agilent 7700 quadrupole ICP-MS housed at the CODES LA-ICP-MS analytical facility (University of Tasmania, Hobart, Australia). The analyses of a isocubanite–chalcopyrite aggregate from sample 219 include only ^{49}Ti, ^{51}V, ^{53}Cr, ^{55}Mn, ^{57}Fe, ^{59}Co, ^{60}Ni, ^{65}Cu, ^{66}Zn, ^{75}As, ^{77}Se, ^{95}Mo, ^{107}Ag, ^{111}Cd, ^{118}Sn, ^{121}Sb, ^{125}Te, ^{182}W, ^{197}Au, ^{205}Tl, ^{208}Pb, ^{209}Bi, and ^{238}U.

The analyses were performed by ablating spots ranging in size from 40 to 60 μm. Laser repetition rate was 5 Hz and laser beam energy at the sample was maintained between 4 and 5 J/cm^2. The analysis time for each spot was 100 s, comprising a 30-s measurement of background (laser off) and a 70-s measurement with laser on. The acquisition time for all masses was set to 0.02 s. Calibration was performed using GSD-1G (GeoRem preferred values) and STDGL2b2 [27], an in-house reference material specifically developed to enable LA-ICP-MS analysis of chalcophile and siderophile elements in sulphide minerals. The accuracy of LA-ICP-MS analyses calibrated on STDGL2b2 reference material using the above analytical conditions is demonstrated to be better than 15–20% [27]. To account for the instrument drift, the standard was analyzed twice every one hour and a half, using a 100 μm beam and a repetition rate of 10 Hz, thus closely maintaining the aspect ratio between ablation craters on the samples and on the standard. Data reduction was undertaken according to standard methods [28]. Iron was used as the internal standard for quantification of sulfides. Concentrations of the internal standard were calculated assuming stoichiometry. The detection limits were calculated as three times the standard error for the count rates of the instrument background signal (laser-off). The LA-ICP-MS analyses were processed in the Statistica v. 10 program using correlation analysis, in order to identify

trace element associations, which were ordered from maximum to minimum coefficient of correlation according to method of [29]. The correlation matrices at confidence level of 95% are presented as Table S1.

The formation of mineral assemblages of the studied samples was also examined using thermodynamic modeling. Its initial parameters are based on sulfide mineralogy, so the details of the modeling are provided after the mineralogical descriptions in Section 5.3.

4. Results

4.1. Textures and Mineralogy of Sulfides

4.1.1. Station 233

Cu-rich massive sulfide sample 233-3 exhibits cavernous and porous structure (Figure 2a) and relatively simple mineral composition with variable amount of major covellite (~50–70 vol %) and abundant isocubanite and pyrite (~50–30 vol % in total). According to XRD, the sample also contained minor (<1 wt %) chalcopyrite, marcasite, atacamite, serpentine, and quartz, as well as natrochalcite $NaCu_2(SO_4)_2(OH) \times 2H_2O$ and bonattite ($CuSO_4 \times 3H_2O$), the presence of which is most likely related to the laboratory oxidation of samples.

Under an optical microscope, covellite forms massive aggregates, which nearly completely replace crystalline isocubanite (Figure 2b). Tiny (1–5, rarely, 20–30 μm in size) pyrite crystals overgrow isocubanite–covellite aggregates and form thin (a few micrometers thick) veinlets in them (Figure 2b). Rare radial crystalline aggregates of gangue minerals (possibly atacamite) are observed on top of some isocubanite crystals. The sulfide aggregates are locally covered by a thin (1–5 μm thick) discontinuous quartz rim. Extremely small (~1 μm in size) hexagonal and triangle crystals of native gold were found in covellite and at the isocubanite–covellite contact (Figure 2c,d). Native gold in covellite contains 0.76 wt % Ag and that at the isocubanite–covellite contact has higher Ag content (3.64 wt %) (Table 2).

Table 2. Chemical composition of some accessory and rare minerals of the Ashadze-2 hydrothermal field, wt %.

Laboratory Number of Analysis	Au	Ag	Pb	Zn	Fe	Cu	Se	S	Total
Sphalerite									
27085a				58.63	6.56	0.89		33.34	99.42
27085d				59.03	6.40	0.65		33.31	99.39
Clausthalite									
27085b			74.43				22.21	2.75	99.38
27085c			73.00				23.72	2.54	99.26
Galena									
27085e			76.60	4.88	2.19			15.42	99.10
Native Gold									
27086c *	99.24	0.76							100.00
27086b *	96.36	3.64							100.00
27089a	92.65	7.35							100.00

Due to extremely small size of grains and elements captured from host sulfides, the analyses of native gold are recalculated to 100 wt %. Empty cells, not detected; *, analyses 27086c and 27086b, sample 233-22; other analyses, sample 240-2.

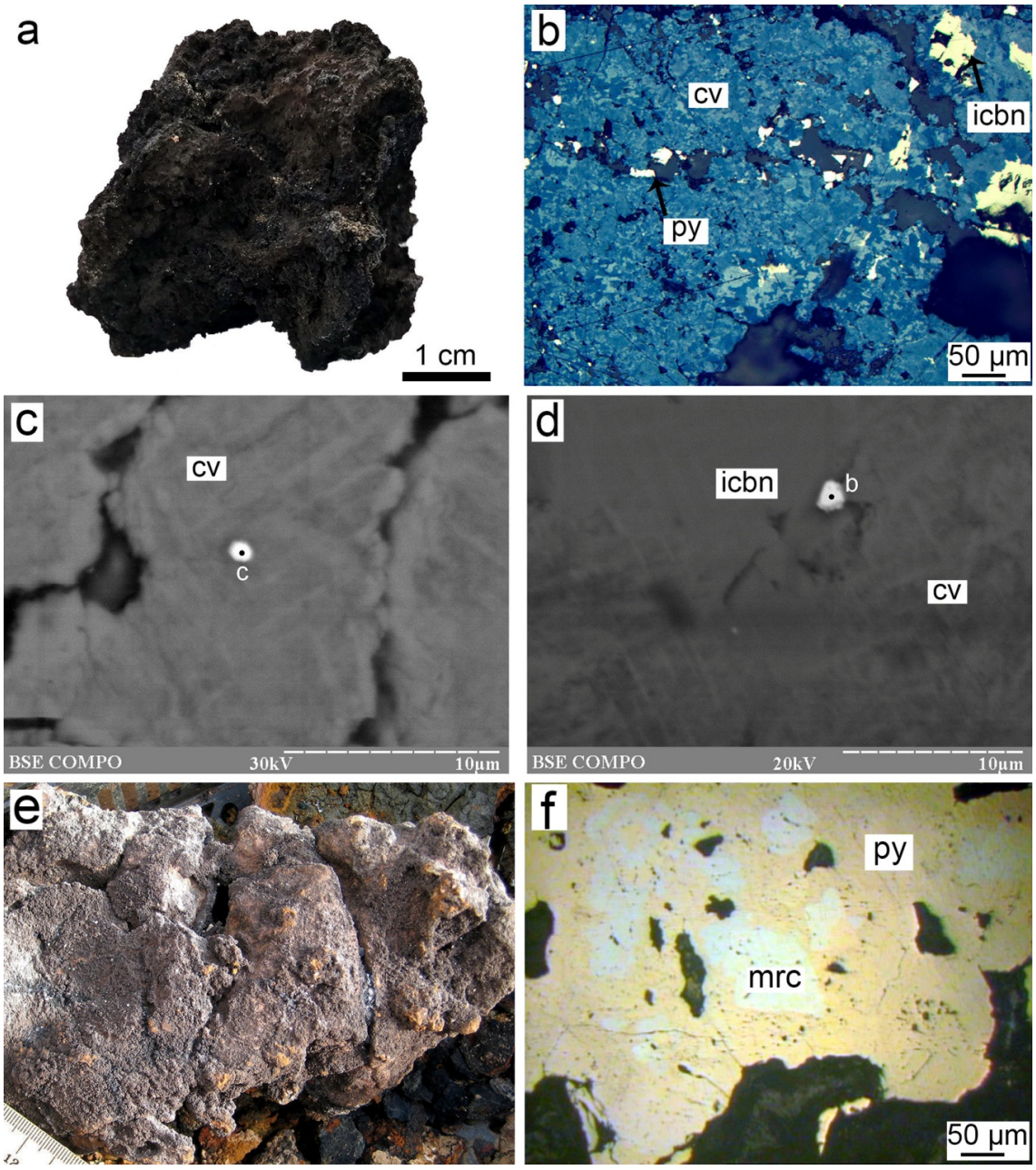

Figure 2. Cu-rich (**a**) and Cu-bearing Fe-rich (**e**) massive sulfide samples from station 233 (on-board photographs); crystalline isocubanite (icbn) almost completely replaced by covellite (cv) and overgrown by crystalline pyrite (py) (**b**); native gold in covellite (**c**, point c) and at the isocubanite-covellite contact (**d**, point b); zonal marcasite(mrc)–pyrite aggregates (**f**). Photos (**b**,**f**), reflected light; (**c**,**d**), SEM images. Hereinafter, the mineral abbreviations follow the recommendations of [30], except for isocubanite, native gold, and clausthalite (see below).

In massive Cu-bearing sample 233-22 (Figure 2e), major marcasite and pyrite (~50% in total) are developed around less abundant chalcopyrite (~30%) and pyrrhotite (~20%) (Figure 2f). Marcasite and pyrite form large (150–250 μm in size) zonal aggregates, where spear marcasite crystals in the center are rimmed by crystalline pyrite. The latter contains numerous pores and inclusions of chalcopyrite and gangue minerals. Some pyrite aggregates exhibit traces of radial structure emphasized by porosity. These structures could have been the relics of former colloform aggregates of Fe disulfides (Figure 2f). In this sample, covellite also replaces Fe sulfides forming very porous mesh aggregates.

4.1.2. Station 240

Cu-rich massive sulfide sample from station 240 exhibits a zonal structure with massive chalcopyrite-rich zone 1, massive bornite-rich zone 2 and porous bornite-rich zone 3 (Figure 3a). The major minerals are chalcopyrite (~40%) and bornite (~30%); sphalerite (~20%) and pyrite (~10%) are secondary in abudance; accessory galena, clausthalite, and native gold are observed as single grains.

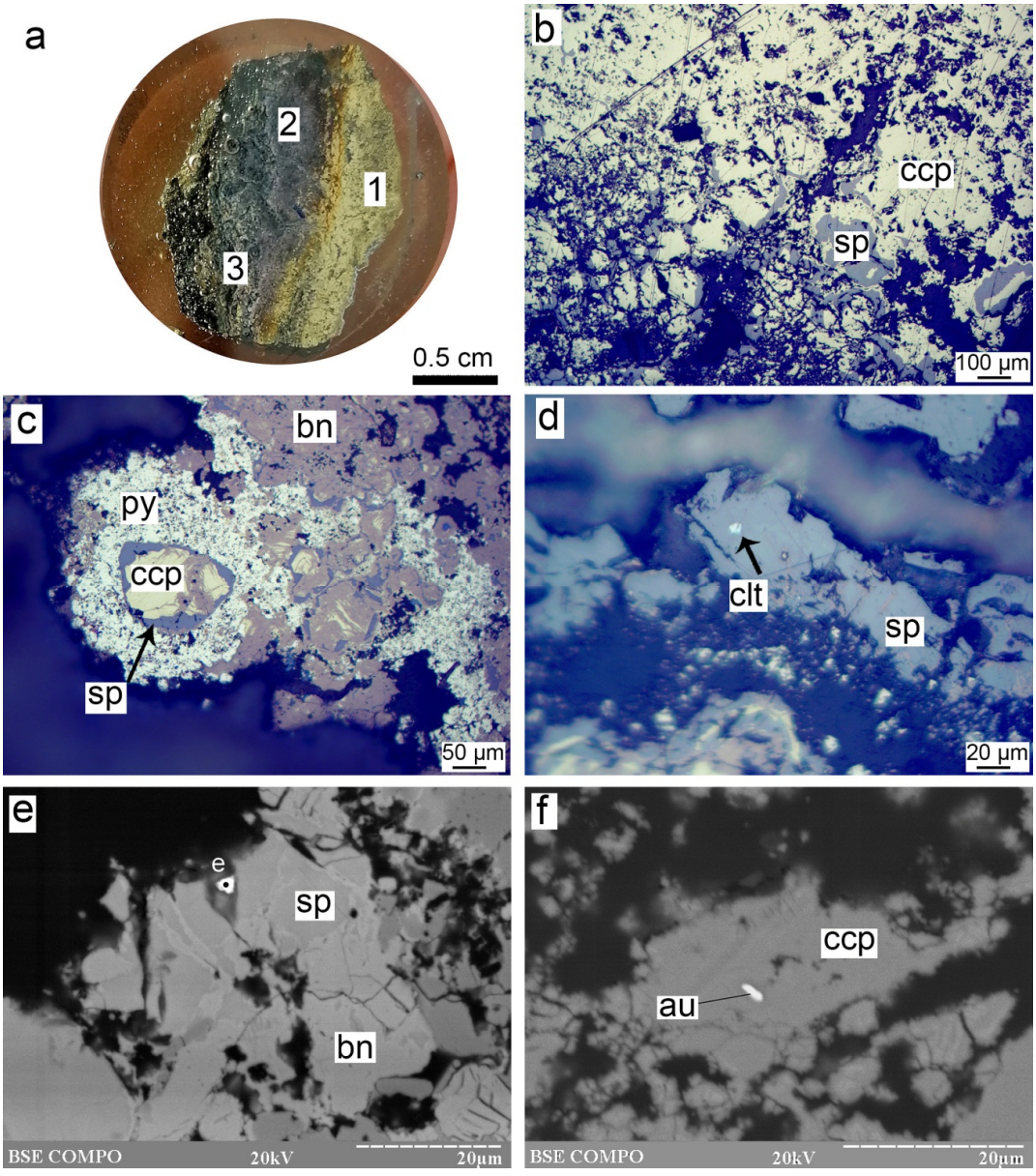

Figure 3. A possible fragment of small Cu-rich chimney from st. 240 with massive chalcopyrite-rich (1), massive bornite-rich (2), and porous bornite-rich (3) zones; (**a**, polished section) massive chalcopyrite (ccp) of zone 1 overgrown by sphalerite (sp) (**b**); chalcopyrite crystals in zone 2 overgrown by sphalerite and fine-grained pyrite and replaced by bornite (bn) (**c**); clausthalite (clt) inclusion in sphalerite of zone 2 (**d**); galena grain (point e) in sphalerite replaced by bornite (**e**); native gold grain in chalcopyrite (**f**). Photos (**b**–**d**), reflected light; (**e**,**f**) SEM images.

The inner zone (zone 1) ~5 mm thick is dominated by massive chalcopyrite aggregates, which are overgrown by sphalerite (Figure 3b). Toward the margin of the inner zone, one can observe individual well-formed chalcopyrite crystals, growing inward. Interstitions between massive chalcopyrite aggregates are filled with fine-grained (a few micrometers) chalcopyrite intergrowths. Sphalerite is characterized by a "chalcopyrite disease" (inclusions of ~1 μm and less) [31] and fine (~1 μm thick) chalcopyrite veinlets. The amount of sphalerite increases toward zone 2. Pyrite occurs in zone 1 as rare small (~10 μm) crystals and, similarly to sphalerite, its amount becomes higher in zone 2.

Zone 1 gradually transits to zone 2 up to 1 cm thick, which is dominated by bornite. In the transition area, bornite forms thin (~5 μm thick) veinlets, which are developed in chalcopyrite aggregates along the crystal boundaries or cleavage. In zone 2, bornite extensively replaces both chalcopyrite and sphalerite and, in turn, is replaced by covellite (Figure 3c). In zone 2, rare sphalerite crystals overgrowing chalcopyrite exhibit an ideal hexagonal shape in the section suggesting the former presence of würtzite. According to SEM EDS analyses, sphalerite contains relatively moderate Fe contents (~6 wt % or ~11 mol % FeS) and low (<1 wt %) Cu contents (Table 2).

Pyrite is much more abundant in zone 2, where it occurs as numerous inclusions in relict chalcopyrite or forms large fine-grained or fine-crystalline aggregates around sphalerite–chalcopyrite intergrowths (Figure 3c). This zone also contains chalcopyrite-2, which overgrows late pyrite as thin continuous rims. Small (5 μm) clausthalite grains are found in sphalerite (Figure 4d). Clausthalite contains S in composition (Table 2). Small galena grains are confined to the fractures in sphalerite (Figure 3e). Galena exhibit traces of Zn and Fe in composition (Table 2). A tiny (2 μm long and 1 μm wide) elongated native gold grain is found in chalcopyrite (Figure 3f). It contains 7.35 wt % Ag (Table 2). Small (<10 μm) interstitial tabular barite crystals are occasionally found in zone 2. The zonal structure of this sample, the inward growing chalcopyrite crystals, and the increasing amount of bornite toward the outer zones indicate that this sample can be referred to as a smoker chimney fragment.

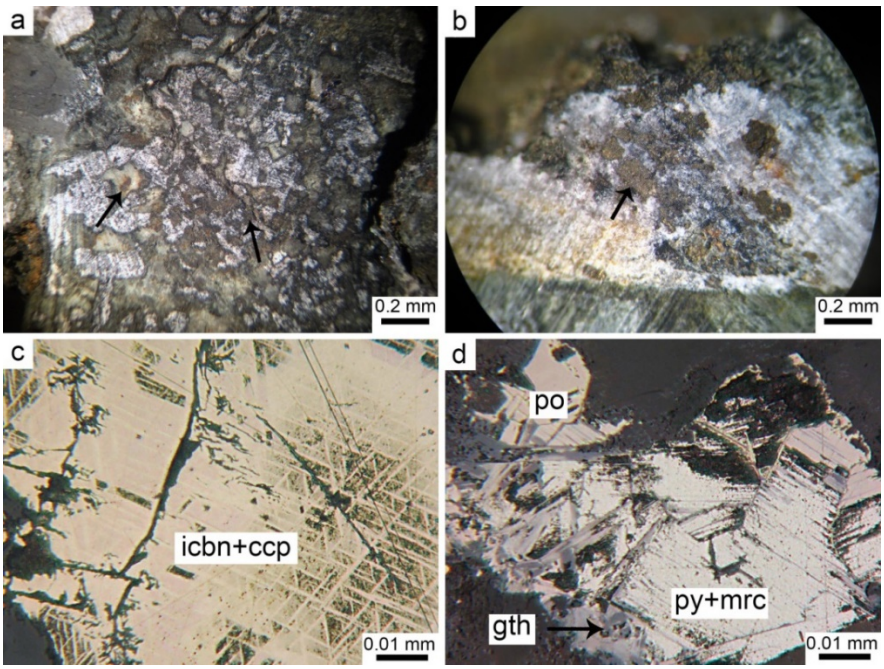

Figure 4. Disseminated Cu–Fe sulfides (indicated by arrows) in strongly altered gabbro with aragonite veinlets (white) (**a**,**b**); isocubanite)–chalcopyrite aggregate with typical lattice structure (**c**); crystalline pyrrhotite (po) replaced by fine pyrite–marcasite aggregates and rimmed by goethite (gth) (**d**). Photos (**a**,**b**), binocular microscope; (**c**,**d**), reflected light.

4.1.3. Station 219

The studied sample from station 219 is a strongly oxidized and altered piece of gabbro with numerous patchy sulfide aggregates, aragonite veins, and abundant crystals of minerals of the atacamite group (Figure 4a,b). Sulfides mostly include aggregates of intimately intergrown isocubanite and chalcopyrite with exsolution lattice structure (Figure 4c). Less abundant pyrrhotite makes up the crystalline aggregates, which are replaced by box-like pyrite–marcasite intergrowths and by goethite from the rims and along the crystal boundaries (Figure 4d).

4.2. Trace Element Composition of Sulfides

The TE composition of sulfides can be found in Table S1. For convenience of the description, the TE contents are subdivided into relatively high (>1000 ppm), elevated (100–1000 ppm), moderate (10–100 ppm), and low (<10 ppm). Below, we describe and further discuss the composition of minerals based on median values if not specified. Since all sulfides are characterized by variable amount of "rock-forming" elements (Mg, Al, Si, Ca) (Table S1), which are related to the inclusions of gangue minerals, we omit their presentation in Results, but use them in Discussion to help in the understanding of TE associations.

Pyrite from sample 233-1 is characterized by high Cu, elevated Mn, and moderate V, Co, Zn, As, Mo contents. The contents of most other elements (Ti, Cr, Ni, Ga, Se, Sr, Ag, Cd, In, Sn, Sb, Te, Ba, W, Au, Tl, Pb, Bi, and U) are low. Covellite, which replaces pyrite (hereinafter, covellite-A for simplicity) or most likely a mixture of Fe sulfides (a laser beam could have caught small inclusions of marcasite and pyrhhotite in pyrite), exhibits high Fe, and moderate V, Zn, Se, Ag, and Pb contents (Figure 5, Table S1). The contents of Ti, Cr, Mn, Co, Ni, Ga, As, Sr, Mo, Cd, In, Sn, Sb, Te, Ba, W, Au, Tl, Bi, and U are low.

Isocubanite from sample 233-22 has high Co and Zn, elevated Se, moderate Ag, Sn, and Te, and low Ti, V, Cr, Mn, Ni, Ga, As, Sr, Mo, Cd, In, Sb, Ba, W, Au, Tl, Bi, and U contents. Covellite, which is developed after isocubanite (hereinafter, covellite-B for simplicity), is characterized by high Fe, elevated Se, and moderate Co, Zn, As, Ag, Sn, and Te contents (Figure 5, Table S1). The amount of Ti, V, Cr, Mn, Ni, Ga, Sr, Mo, Cd, In, Sb, Ba, W, Au, Tl, Bi, and U is low.

Chalcopyrite from sample 240-8 is characterized by high Co contents, elevated amounts of Ni, Zn, and Se, and moderate contents of Ag, Sn, and Te (Figure 5, Table S1). Other elements show low contents. Bornite, which replaces chalcopyrite, has high Co and Se, elevated Ni and Zn, moderate Ag, Sn, and Te contents, and low concentrations of other elements (Figure 5, Table S1). Isocubanite + chalcopyrite mixture from station 219 has high Co, Ni, and Zn, elevated Sb, and moderate As, Se, Mo, Cd, Sn, Tl, and Pb contents (Figure 5, Table S1). The contents of Ti, V, Cr, Mn, Ag, Te, Ba, W, Au, Bi, and U are low.

Comparing to each other, pyrite of the studied Ashadze-2 samples is a main carrier of Mn; covellite-A accumulates V, Ga, In, Ba, and W; isocubanite is characterized by the highest Co contents; covellite-B is host to the highest Sr, Ag, and Bi contents; chalcopyrite concentrates most Au and U; bornite has the highest amounts of Se, Sn, and Te; and isocubanite+chalcopyrite mixture contains the highest amounts of Ni, Zn, As, Mo, Cd, Sb, Tl, and Pb (Figure 5, Table S1).

In comparison with pyrite, covellite-A is enriched in V, Cr, Zn, Ga, Se, Sr, Ag, Cd, In, Sn, Sb, Te, Ba, W, Au, Tl, Pb, Bi, and U (Figure 5, Table S1)., Covellite-B is enriched in Mn, Ga, As, Se, Sr, Mo, Ag, Sn, Sb, Ba, W, Au, Tl, Pb, Bi, and U relative to isocubanite (Figure 5, Table S1). Bornite after chalcopyrite is enriched in Ti, Co, Ga, Se, Ag, In, Sn, Sb, Te, and Bi relative to chalcopyrite (Figure 5, Table S1).

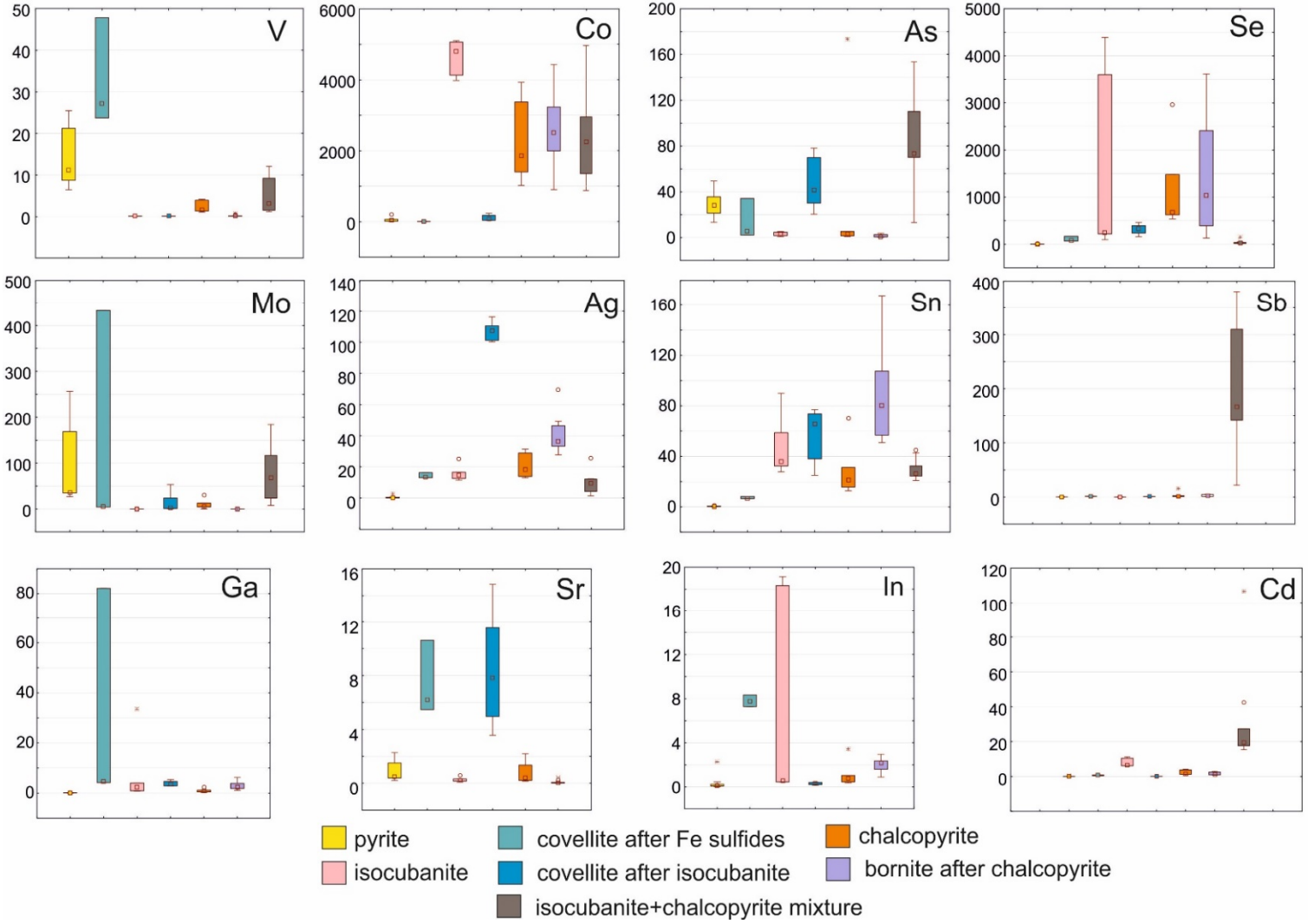

Figure 5. *Cont.*

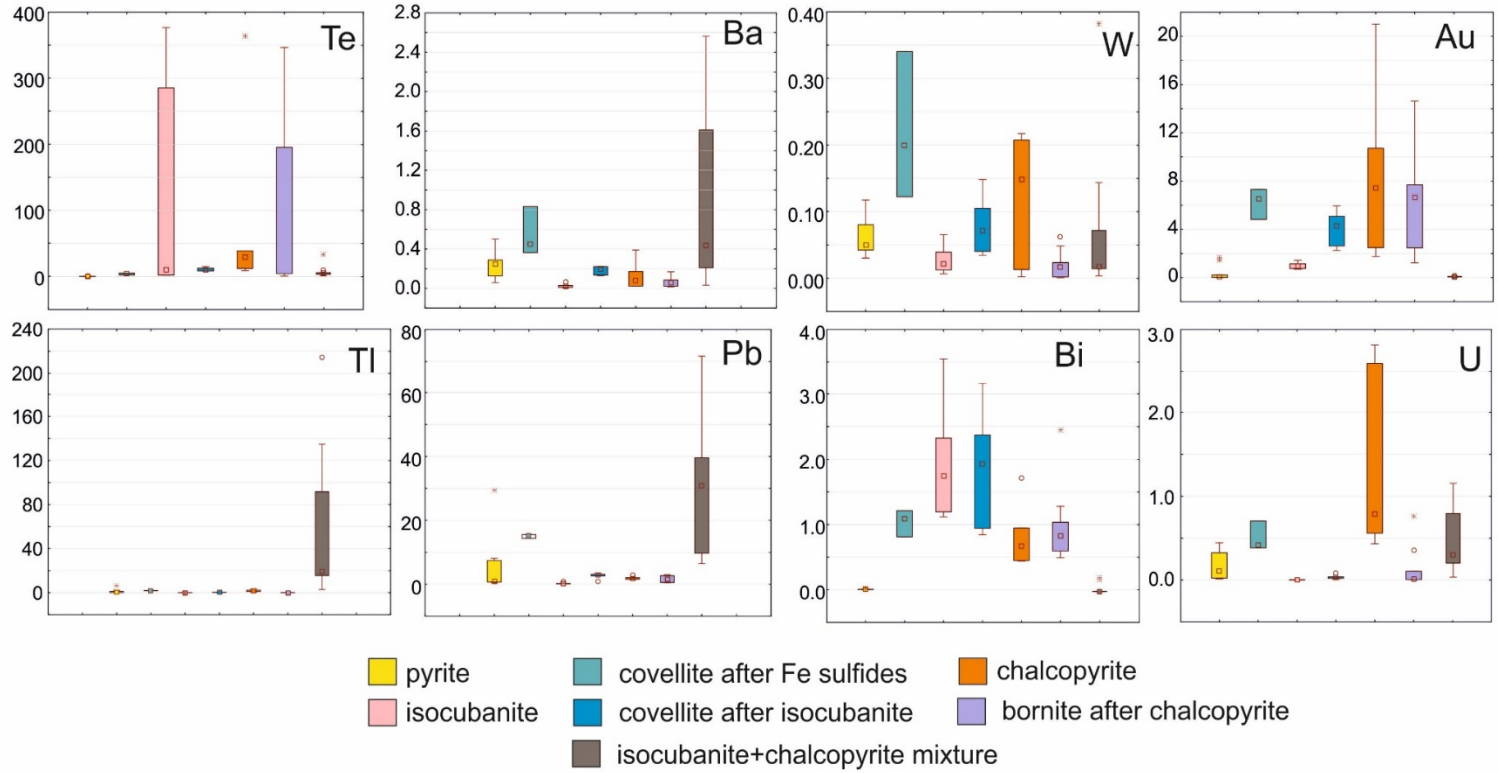

Figure 5. Box-and-whisker plots for selected trace elements (ppm) in sulfides of the Ashadze-2 hydrothermal field.

4.3. Physico-Chemical Modeling

According to the LA-ICP-MS analysis, covellite is enriched in many TEs including Au and Pb. To assess the possible role of seawater in enrichment in Au, Pb, and a number of other TEs of covellite, we simulated the process of its seawater-affected formation using thermodynamic modeling. The modeling was conducted by Gibbs energy minimization using a flow reactor model in the Selektor program [32]. The modeling uses a matrix of dependent components and thermodynamic parameters, which have been published in [12,13]. The composition of seawater is given according to [33]. The Ashadze-2 hydrothermal field occurs at depth of 3200 m (see above), thus the pressure in modeling is accepted as 33.8 MPa. Both seafloor samples from stations 233 and 240 contain covellite and Au- and Pb-bearing accessory minerals, so the starting composition of massive sulfides (Table 3) for modeling approximately corresponds to their average composition.

Table 3. Model composition of massive sulfides.

Mineral	Formula	Vol%	Mole/kg
Isocubanite	$CuFe_2S_3$	~30	0.988745
Chalcopyrite	$CuFeS_2$	~30	1.593732
Bornite	Cu_5FeS_4	~25	0.575394
Sphalerite	ZnS	~10	0.956737
Pyrite	FeS_2	~5	0.4760325
Galena	PbS	0.003	0.0000721
Clausthalite	PbSe	12 ppm	0.0000349
Native gold	Au	5 ppm	0.0000254

The volume percent of galena and native gold correspond to the minimum Pb and Au contents identified by chemical analysis of bulk samples (see above). No data are available for Se contents of Ashadze-2 massive sulfide samples, thus the Se content was accepted 12 ppm, which is the lowest Se contents determined for the Ashadze-1 hydrothermal field [24].

The starting modeling temperature was 350 °C, which is a typical temperature of black smokers [34]. This temperature could have been achieved by the Ashadze-2 fluids, which is indicated by the presence of isocubanite and pyrrhotite and high Se contents of isocubanite and chalcopyrite (see Discussion). Two additional modeling runs with different starting temperatures are also conducted to support our main modeling procedure: (i) starting temperatures of 400 °C were chosen because of the temperature documented at the Turtle Pits hydrothermal field, MAR (of up to 400 °C and more [35]); and (ii) starting temperatures of 296 °C were measured at the Ashadze-2 hydrothermal field [23]. The results of modeling run (i) are similar with those with temperature of 350 °C, whereas the modeling run (ii) yields negligible amount of covellite. This is explained by the decreased solubility of Cu minerals, which significantly drops in temperatures below 350 °C [36]. This result also indirectly supports the conclusion of [23] on an underestimated temperature of 296 °C, as a result of unstable position of remotely operated vehicle at the bottom of the crater during the measurement, and that the true temperature is therefore probably higher.

It was previously shown on example of a black smoker from the Endeavour segment of the Juan de Fuca Ridge that the internal pressure in a fluid flow is lower than the external pressure [37]. Therefore, in case of open porosity of massive sulfides, seawater would penetrate inside and the degree of its pumping depends on the permeability of the substrate [37]. Since the massive sulfide edifice is heated by a deep fluid, seawater would also be heated, possibly, up to the temperature of the inner chimney wall. This was the basic principle of the modeling of massive sulfide/heated seawater interaction at the Ashadze-2 hydrothermal field.

The first modeling stage included a revision of equilibrium mineral assemblages and element contents in solution at different massive sulfides/seawater (MS/SW) ratios for 350 °C (Figure 6). As follows from the calculations, the low MS/SW ratios are favorable for oxidizing conditions of the system (Eh > 0.52 V) and the precipitation of hematite. The increase in MS/SW ratio results in the change of redox conditions ($\xi = -\log_{10}(MS/SW) = 4.96$) and crystallization of sulfides due to saturation

conditions. Native gold and clausthalite in the model are registered at ξ > 2.09 and >1.04, respectively. pH of the system for 350 °C remains constant (5.2–5.35) for the entire range of the MS/SW ratio.

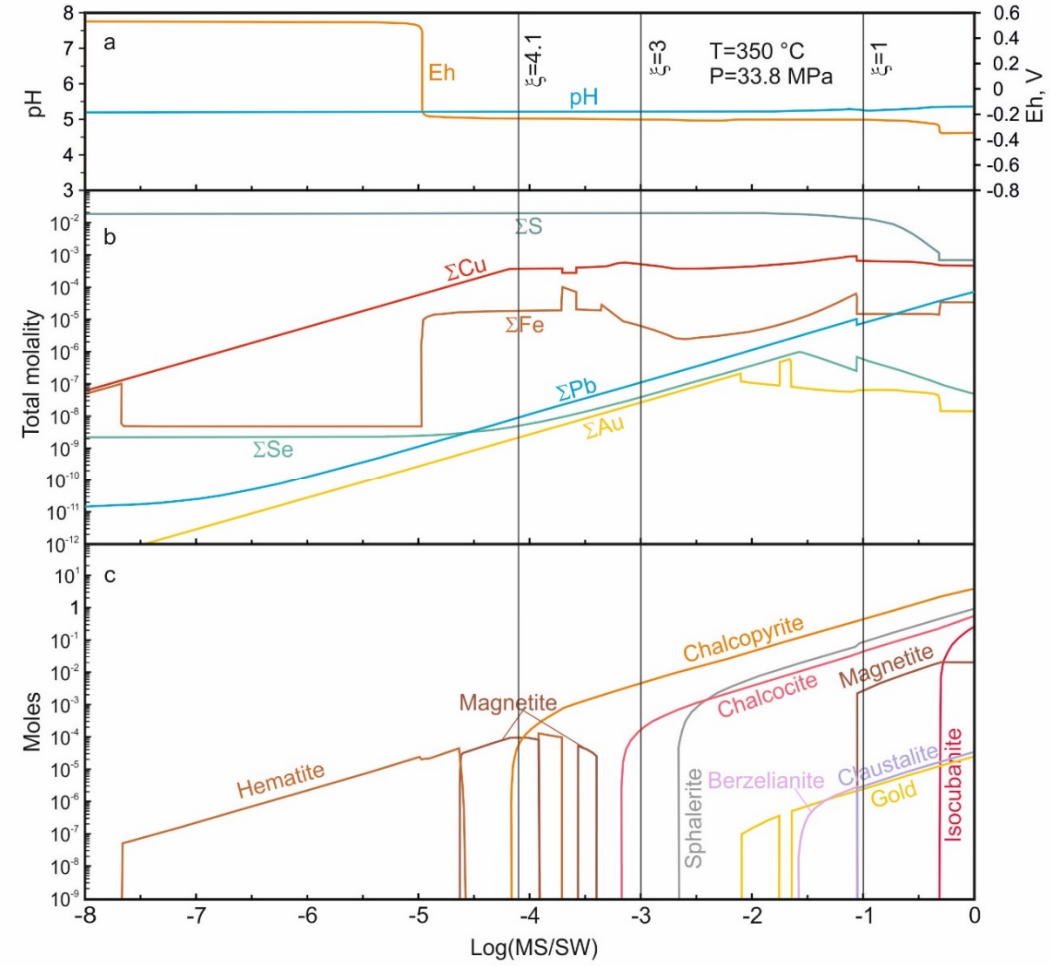

Figure 6. Calculated pH (**a**) element content in solution (**b**) and mineral assemblages (**c**) precipitated as a result of massive sulfides/seawater (MS/SW) interaction. Vertical lines corresponds to ξ values ($-\log_{10}$(MS/SW)), for which mineral assemblages at conductive cooling are calculated (see figures below).

On the basis of these results, we chose three MS/SW ratios for modeling of conductive cooling of the solution (Figure 6). The ξ value of 4.1 occurs in the area of saturation with respect to Cu sulfides and ξ values of 3 and 1 reflect the increasing MS/SW ratio, and correspond to the increasing time of a circulating fluid in the sulfide edifice. These models are based on a flow reactor method, when a mobile reacted phase (in our case, solution) moves from one system to another under variable depending components and external system parameters (temperature and pressure) [38]. In the model, seawater was heated up to 350 °C, interacted with massive sulfides, and was then gradually cooled with a step of 10 °C to the temperature of ambient seawater (2 °C).

Seawater heating includes two scenarios: (1) heating up to 350 °C and reaction with massive sulfides in the second reservoir (Figure 7a) and (2) gradual heating with a step of 50 °C and reaction with massive sulfides after each 50 °C (Figure 7b). In both cases, chalcopyrite and chalcocite are the most high-T minerals precipitated from the solution at ξ values of 4.1 and 3 (Figure 7a,b), which is evident of early saturation of the solution with respect to Cu. At the ξ value of 1, these minerals are accompanied by sphalerite, clausthalite, and native gold under high-T conditions; however, the calculation for the ξ value of 1 is inconsistent with natural mineral assemblage, because sphalerite generally precipitates at lower temperatures [39].

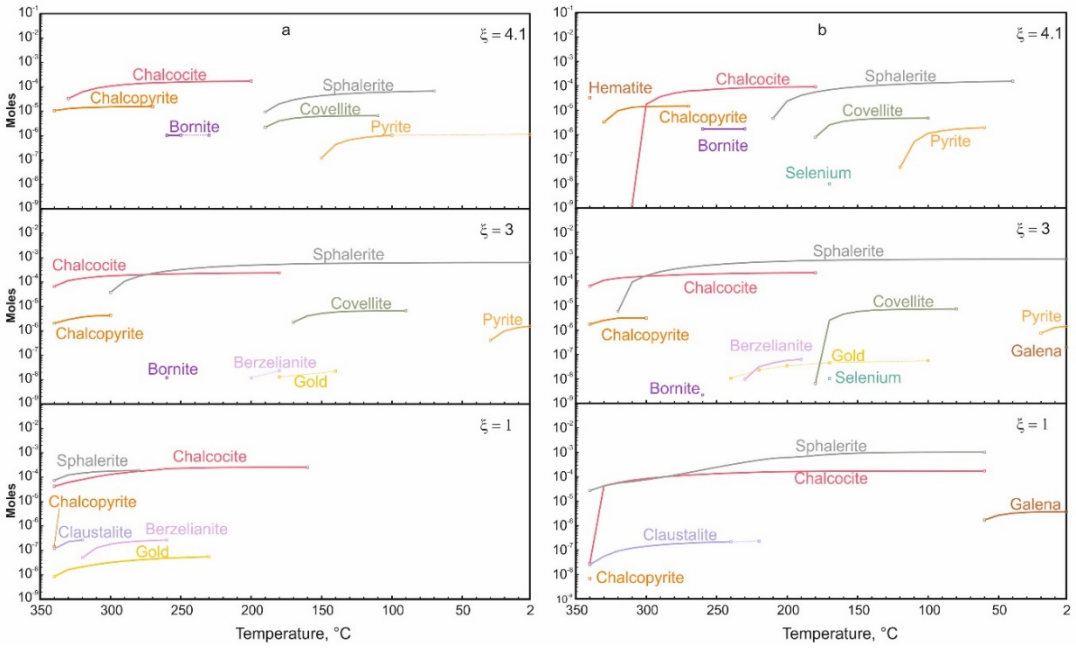

Figure 7. Calculated mineral assemblages precipitated as a result of MS/SW interaction and conductive cooling for various MS/SW ratios: scenario 1 (**a**) and scenario 2 (**b**); the figure shows only areas with decreasing temperature). Dotted line, the mineral is absent in the corresponding range.

The increasing MS/SW ratio in the solution results in accumulation of TEs (in our case, Pb, Se, Au), which are extracted from an enhanced amount of primary massive sulfides, and are precipitated as accessory and rare minerals (clausthalite, berzelianite, native gold). Pyrite precipitates under low-T (<150 °C) conditions and a low MS/SW ratio (ξ value = 4.1, Figure 7a,b). Covellite is stable in a temperature range of 190–90 °C at a ξ value between 3 and 4.8 (Figure 7). No covellite forms at higher MS/SW ratios. The temperature of its crystallization can increase up to 220–230 °C in the presence of pyrrhotite and higher amount of pyrite (our unpublished data).

The maximum Au concentration in the solution in of scenario 1 is 2.02×10^{-7} mol/kg H_2O at ξ value of 2.1 (Figure 6). In a conductively cooling solution, Au achieves concentrations of saturation and precipitates at ξ value of >3.9. In oxidizing conditions (ξ value > 4.6), hematite is stable (Figure 7). The model of mineral precipitation following conductive cooling for this area shows the formation of higher-T hematite and lower-T goethite and tenorite.

The modeling principles of equilibrated mineral assemblages allow no discussion of the replacement processes at equal temperature. In case of the lower-T mineral assemblage, however, we suggest that new minerals can replace those previously precipitated. This means that covellite and pyrite are the final products of the replacement of Cu- and Fe-bearing sulfides under reducing conditions, in contrast to Fe-oxyhydroxides and Cu oxides and carbonates under oxidizing conditions.

No chalcocite is reported from the Ashadze-2 massive sulfide samples, in contrast to the modeling results. This difference can be related to inaccurate thermodynamic constants for high temperatures or kinetic parameters, which significantly affect the equilibrium conditions of mineral precipitation. No berzelianite was found in our samples; however, its formation in the modeling is expected due to initial Se contents. In studied Ashazde-2 samples, Se is present as TE in sulfides, but modeling cannot take into account the isomorphic state of elements in minerals.

5. Discussion

5.1. Mode of Occurrence of Trace Elements in Sulfides

The TEs in minerals can occur as isomorphic substitutions, absorbed mode, or inclusions of other minerals. In spite of visually "clean" analytical area under an optical microscope, the entrapment of nano-sized or deep-seated inclusions of other minerals is expected during LA-ICP-MS analysis. Correlation analysis both of major (Fe, Cu) and trace elements, which are ranged from maximum to minimum correlation coefficients, can elucidate and predict the mode of occurrence of TEs, as well as their possible origin and factors controlling their distribution [2]. Each mineral analyzed of the Ashadze-2 hydrothermal field exhibit specific elemental association (further, association) indicating different mode of occurrences of TEs.

5.1.1. Pyrite, Station 233

Pyrite from sample 233-1 has nine associations: I (Co–Ni–Ag–In)–II (Pb–Tl–Cd)–III (Mg–Cu–Se), IV (Mn–Au)–V (Mo–V–Ga); VI (Sr–Ba); VII (As–Sb); and VIII (Al–Cr–U)–IX (Sn–Ca) (hereinafter, positively correlated elements are connected by dash; for correlation coefficients, see Table S1). Association I consists of Co, Ni, Ag, and In. Cobalt and Ni are typical TEs of pyrite, which isomorphically substitute Fe [40]. It was reported on the presence of Ni- and Ag-bearing (but no Co-bearing) nanoparticles of Au–Ag–As–Ni–S, Fe–As–Ag–Ni–S, and Fe–As–Sb–Pb–Ni–Au–S composition in pyrite from various continental deposits [41]. In our case, we suggest the isomorphic state of Co and Ni in pyrite, which is supported by their high correlation (Table S1). Silver and In are more characteristic of chalcopyrite or sphalerite [6,10,40], which frequently occur as inclusions in pyrite, as well as the nanoparticles of above composition [41]. In our case, Ag and In exhibit high correlations with Co and Ni pointing to a possible isomorphic state. At least, it was suggested that trivalent In could substitute to arsenious pyrite in a manner similar to Tl or Au [40].

Association II includes a suite of toxic TEs (Pb, Tl and Cd), which are correlated with TEs from association I. It is considered that Pb and Cd in pyrite most often occur as nanoparticles of galena and sphalerite, respectively [7,40,41], whereas Tl in pyrite can be a nonstoichiometric trace [40,42]. Thallium, however, is a common trace of galena and sphalerite too [4,7]. Assuming generally low contents of Pb, Tl, and Cd and their high correlations with Co and Ni, we can speculate on their nonstoichiometric substitution in pyrite lattice. At the same time, we cannot rule out the presence of Tl- and Cd-bearing galena, because of analysis ma23a075, which exhibits a maximum of Pb, Tl, and Cd contents (Table S1).

Association III has three correlated elements, two of which (Cu and Se) account for Se-bearing chalcopyrite (Table S1) inclusions in pyrite. Their correlation with Mg may indicate the association of chalcopyrite with talc, which is common at the Ashadze-2 field [22].

Association IV exhibits high correlation between Mn and Au. Manganese, along with Co and Ni, can substitute Fe in the crystal lattice of pyrite. Strongly variable Mn contents (45.34–9402 ppm; Table S1), however, are better consistent with Mn-bearing inclusions [42], most likely, Mn hydroxides, which are essential components of seafloor hydrothermal fields [39]. Manganese often enriches low-T colloform varieties of pyrite, as well [2]. The presence of relict colloform structures is suggested for the inner zones of some pyrite crystals (Figure 2d), thus Mn-bearing inclusions could have been inherited from former colloform Fe disulfides similarly tp early fine-crystalline and framboidal pyrite from the Semenov-1 hydrothermal field (MAR) [13]. This may indicate similar entrapment mechanism of Mn and Au under relatively low-T seawater-affected conditions (cf. [2]). The latter fact is in agreement with related association V, which includes seawater-sourced Mo and V [43]. Positive Mn–Mo correlation (Table S1) indicates that Mo (as well as V) could have been absorbed by Mn hydroxides [2]. Having Ga in association V, we can speculate on Ga absorption by Mn hydroxides similarly to Ga-bearing Mn nodules [44].

Association VI indicates the presence of barite inclusions. The As–Sb correlation in association VII suggests nonstoichiometric substitutions for S [40,45], since the microinclusions of As- and Sb-bearing minerals are unexpected due to low and very uniform concentrations of As and Sb in pyrite. Associations VIII combine TEs most likely reflecting the presence of U-bearing smectites (Al, Cr). Association IX with Ca can reflect the possible presence of traces of anhydrite in assemblage with chalcopyrite; both Ca and Sn have correlations with elements from association III.

A number of TEs are incorporated in no associations, and this could be because of several reasons: (i) they have negative correlations, whereas associations are based on positive correlation values: Fe is negatively correlated with all TEs from associations I–III or Bi is negatively correlated with V and Mo; (ii) they exhibit much lower correlations with other TEs: e.g., Te is correlated with Sn (r = 0.72; Table S1). Similarly, W is correlated with Mn (r = 0.75; Table S1), however, this correlation is masked by higher Mn–Au one; (iii) they also occur as inclusions, e.g., quartz (Si), sphalerite (Zn), or anatase (Ti). The latter is a typical alteration product of volcanic glass [46], however, its presence in chimney material in form of low-T precipitate is reported from the Southern Juan de Fuca Ridge [47].

Some TEs probably can be of dual origin: the analysis ma23a075 with relatively high Pb, Tl, and Cd contents (Table S1) is also characterized by the highest Cu contents accompanied by a maximum of Co and Ni contents, which are responsible for the entrapment of most likely Co–Ni bearing chalcopyrite. Although Ag and In are incorporated in association I due to their high correlation with Co and Ni, they also exhibit high correlation with Cu and Sn indicating their incorporation in chalcopyrite inclusions (see below).

5.1.2. Isocubanite, Station 233

Isocubanite exhibits nine associations: I (Ga–Tl)–II (Ag–Cu)–III (Ca–Sn); IV (Se–Te–Cd–In)–V (Ti–Zn); VI (Mg–Bi–Sr); VII (Si–V); VIII (As–W–U); and IX (Al–Mn). Some associations can be explained by isomorphic substitutions (I, II, IV), an absorbed mode of occurrence (VIII), or uniformly distributed inclusions of non-opaque minerals (VI, VII, IX).

Associations I and II consists of elements, which are correlated with Cu and most likely occur as isomorphic substitution [40]. It was recently shown that Ga prefers chalcopyrite in samples of some continental deposits, which underwent high-T recrystallization, whereas, under low-T conditions, it is mainly hosted in sphalerite [48]. The presence of Tl in this association is intriguing, because it typically pertains to lower-T colloform pyrite, marcasite, galena, or sphalerite [2,7]. Nonetheless, high-T minerals such as isocubanite or chalcopyrite can incorporate negligible amounts of Tl in the absence of above mentioned minerals [2,49]. Association III with Ca can be attributed to the possible presence of relict anhydrite inclusions.

Association IV includes Se, Te, Cd, and In, which, similarly to chalcopyrite, are also isomorphic elements substituting S (Se, Te) and Fe (Cd, In) [15,40]. This association is linked to association V with Ti and Zn. The uniform Zn contents and correlation of Zn with Cd and In (which both are correlated with most likely isomorphic Te and Se) can be accounted for substitution of Fe as well, however, its strong correlation with Ti is problematic to explain.

Associations VII and IX can be attributed to the possible inclusions of V- and Mn-bearing smectites. Association VIII combines absorbed seawater-derived [15,43] U, As and, probably, W. Association V can tentatively be explained by inclusions of a Mg- and Sr-bearing carbonate.

Some elements including Fe, Cr, Co, Ni, Mo, Sb, Ba, Au, and Pb are incorporated in no associations for several reasons. Chromium, Ba, Au, and Pb have no correlations with other elements, probably, because of non-uniformly distributed nanoinclusions of Cr-, Ba-, Au-, and Pb-bearing minerals (silicates, barite, native gold, and galena, respectively). Antimony is correlated with As (r = 0.83; Table S1), but this correlation value is lower than that between As and W (Table S1). Nickel exhibits a negative correlation with Si (r = –0.84; Table S1).

Cobalt and Mo exhibit significant negative correlations with many elements (Table S1). Although Co and Ni are more characteristic of Fe disulfides, Cu–Fe sulfides (chalcopyrite and,

probably similarly, isocubanite) can host these elements as solid solutions, especially in the absence of co-crystallized sulfides [49]. The absence of Co–Ni correlation in the Ashadze-2 isocubanite is unusual, since it would suggest their non-isomorphic state. This is in contrast to the isocubanite from, e.g., Semenov-2 hydrothermal field, the chemical composition of which indicates isomorphic state of Co and Ni, due to Co–Fe, Fe–Ni, and Co–Ni correlations: 0.84, 0.65, and 0.91 (the correlation coefficients are calculated from LA-ICP-MS data of [12]). At the same time, uniform distribution of Co contents (Table S1) contradicts the possible presence of inclusions of Co-bearing minerals. Cobalt also exhibits high significant negative correlations with all elements of "isomorphic" association IV (Se, Te, Cd, In), probably, meaning a possible coupled substitution for Fe, which involves In or Cd. This suggestion is indirectly supported by correlation between Fe and sum of Co, Zn, Cd, In, Mo, and Sn (r = 0.72; not shown).

5.1.3. Covellite, Station 233

There are few analyses of covellite-A, so we combined both types of covellite into one correlation matrix, which exhibits seven associations: I (V–U–Mg–Ca–Al–Tl)–II (In–Pb–Cd–Ni)–III (Ga–Mo–W–Au); IV (Co–Bi–Mn–As)–V (Sn–Ag)–VI (Te–Se); and VII (Fe–Ba–Si). The TEs in associations I–III are closely associated and all metals from association II exhibit high correlations with U, V, Mg, Ca, Al, and Tl. This fact, and elevated contents of Mg, Ca, Al and Si in covellite relative to primary sulfides, indicate the assemblage of covellite with phyllosilicates, which can be a good sink for heavy metals (e.g., [50–53]), as well as for seawater-derived U and V [54,55]. A close link between U and phyllosilicates is also supported by the finding of numerous uraninite grains in sepiolite of the Ashadze-2 gossans [26].

Association III with Ga, Mo, W, and Au is also correlated with associations I and II and, similarly to association I, contains seawater-derived Mo [43] and, probably, W [2]. The correlation of Au with Mg, Al, Ca, V, W, Pb, and U indicates its mobilization during the synchronous formation of covellite and phyllosilicates.

Association IV with Co, Bi, Mn and As is rather curious, but can be referred to as co-precipitating particles of Mn oxyhydroxides, which absorb Co, Bi, and As similarly to Fe–Mn nodules and crusts [56–58]. Associations V and VI most likely reflect isomorphic TEs for Cu (Sn and Ag) and S (Te, Se), which is supported by their uniform distribution. Association IV with Fe, Ba, and Si most likely belong to covellite-B, due to the captured inclusions of pyrite, barite, and quartz, assuming highly variable Fe contents in covellite-B (Table S1). Covellite-A is characterized by much less variable Fe contents and high negative correlation of Fe and Cu (r = −0.97; Table S1) supporting partly isomorphic state of Fe in covellite.

Several association-free elements include Ti, Cr, Cu, Zn, and Sr (Table S1). Titanium, Cr, and Sr are atypical TEs of sulfides, and are probably hosted in gangue minerals. Assuming the homogeneous distribution of Zn contents in both types of covellite and an insignificant correlation of Zn and Fe (r = 0.50; Table S1), we can suggest that Zn is also an isomorphic substitute for Cu in covellite.

5.1.4. Chalcopyrite, Station 240

Chalcopyrite exhibits six associations: I (As–Sb–Zn); II (In–Sn–Pb–Se–Te–Bi–Ni–Co); III (Sr–Ba–Mo–Mg–V–Tl–W); IV (Mn–Au–Ti); V (Cd–Cr); and VI (Al–U). Association I most likely reflects the associated inclusions of sphalerite and submicroscopic sulfosalts. This is in line with highly variable Zn contents (up to 5327 ppm, Table S1). According to [40], the Zn concentrations exceeding 2000 ppm are probably a result of microinclusions of sphalerite.

Association II combines a number of TEs, which most likely occur as isomorphic substitutions [40,49], although, e.g., Pb is more peculiar for galena inclusions [40]. In our case, their most likely isomorphic state is supported by relatively homogeneous contents (Table S1). Association III indicates the presence of barite (Sr, Ba) and possible Mg-silicates, which can form during the mixing of high-T hydrothermal

fluid and seawater [39]. Some of TEs from this association (V, Sr, Ba) are positively correlated with Cu (Table S1).

Unexpected association IV with Mn, Au, and Ti in chalcopyrite resembles association IV of pyrite (Mn–Au), again indicating a link between Mn-bearing minerals (most likely, Mn hydroxides) and Au. This link is supported by some indirect evidence. The enrichment in Au (0.81–16.52 ppm Au) is identified for the low-T Fe–Mn crusts and films on the surface of sulfide samples of the Snake Pit and Broken Spur hydrothermal fields, MAR [59]. These Fe–Mn crusts also contain detectable amounts of Ti (0.10–0.26 wt % [59]). The bulk analyses of sulfides from Axial Seamount show the significant Au–Mn correlation (r = 0.60), and it was suggested that Mn-coatings on fossil chimneys from many of the deposits account for the high Mn associated with some gold-rich samples [60].

Association V with Cr and Cd is intriguing, but, assuming that Cr is also positively correlated with Tl (r = 0.77; Table S1), we can suspect their link with association III. Association VI is similar to association VIII of pyrite with Al and U, reflecting the presence of inclusions of U-bearing smectites.

Silver and Ga, which exhibit no correlation with other elements, are potential isomorphic elements, substituting Cu and Fe in chalcopyrite [10,40,49]. They both have homogeneous distribution and relatively low contents, which is in agreement with isomorphic state (Table S1). The lack of correlations can somehow be related to the unmeasured contents of Ge, which played an important role in coupled substitutions in chalcopyrite [61]. Correlation-free Si most likely reflects the presence of quartz inclusions.

5.1.5. Bornite, Station 240

Bornite exhibits nine associations: I (Sr–V–Mg–Ba)–II (Fe–Ag)–III (Tl–Ti–As); IV (Se–Te)–V (U–Mo–Au)–VI (Ni–Co–In); VII (Al–Si); VIII (Cd–Pb); and IX (Zn–Ga). Associations I and III most likely reflect the inclusions of gangue minerals with absorbed V, Tl, and As. Association II combines positively correlated Fe and Ag, which is rather unusual, because the latter in bornite typically occurs as solid solution substituting for Cu [5]. Its isomorphic state in our case is supported by a high negative correlation of Ag and Cu (r = −0.95; Table S1). The positive Fe–Ag correlation may indicate that this substitution involves Fe as suggested, e.g., for chalcopyrite [61].

Association IV with strong positive Se–Te correlation indicates their isomorphic substitution for S [5]. Cobalt, Ni, and In, which can isomorphically substitute for Fe [5], and resides in association VI. These "isomorphic" associations are combined by association V with typical seawater-sourced TEs (U and V), which are also correlated with Au. Associations VII, VIII, and IX indicate the presence of inclusions of smectites, galena, and sphalerite, respectively.

Several elements are incorporated to none of the associations. Copper shows negative correlations to all elements from associations I, II, III, V, and VI, which include isomorphic metals and possibly co-forming gangue minerals. Chromium has negative correlations with Sr from association I and Mo from association V, and can also be attributed to inclusions of gangue minerals. No correlations are calculated for Mn, Sn, Sb, and Bi. The uniform distribution of these TEs and low contents of Mn, Sb, and Bi are unlikely to be related to inclusions of other minerals.

5.1.6. Isocubanite + Chalcopyrite Mixture, Station 219

Isocubanite+chalcopyrite mixture shows six associations: I (Se–Ag–Cd); II (Bi–W–Sn); III (As–Sb–Ni); IV (Ba–Au–U–Ti); V (Cr–Cu); VI (Pb–V). Association I with most likely isomorphic Se, Ag, and Cd is attributed to isocubanite, due to similar association IV in isocubanite from station 233, where Se is correlated with Cd. The correlation between As, Sb, and Ni in association III, strongly varying Ni contents, and the absence of Co–Ni correlation Ni in isocubanite+chalcopyrite mixture, indicate the presence of inclusions of Ni sulfoarsenides. Association IV represents inclusion-related TEs: gangue minerals (barite and a Ti-bearing phase) and an Au-bearing phase.

As a result of an incomplete range of TEs analyzed and a mixture of two minerals, some of these associations have ambiguous interpretations, e.g., associations II with Bi, W, and Sn, association V with

Cr and Cu, or association VI with Pb and V. Associations II and IV may indicate that "ore" TEs are also related to inclusions of gangue minerals, however, association V remains enigmatic.

Some elements (Mn, Co, Zn, Tl) show no correlations, most likely due to an incomplete range of TEs analyzed. Iron has negative correlations with element from associations III and V. Molybdenum can be ascribed to association IV, due to its correlation with U (r = 0.73; Table S1). The positive correlation of Te with Au (r = 0.67; Table S1) can tentatively indicate the presence of calaverite inclusions. The latter, for example, was found in massive sulfides from the Semenov-2 hydrothermal field [62].

5.2. Remarkable Features of TE Composition of the Ashadze-2 Sulfides

5.2.1. Pyrite

Pyrite from our samples is significantly depleted in Co (average (hereinafter, av.) 50.52 ppm) and Ni (av. 1.58 ppm) in comparison with pyrite from many mafic-, ultramafic-, and even felsic-related hydrothermal sulfide fields:

- Mafic-related fields (ppm, average Co and Ni contents, respectively): 110 and 11.8 at Wocan field [17]; 392 and 1.41 at MESO field [9]; 81 and 3 at Broken Spur field; 345 and 9 at Lucky Strike field; 3946 and 3.1 ppm in sulfides from Galapagos Ridge [3];

- Ultramafic-related fields (ppm, average Co and Ni contents, respectively): 374 and 30.5 at Kairei field; 102 and 19.3 at Logatchev field; 269 and 2.28 at TAG field; 602 and 1.12 at 5° S field [9]; 1200 and 1 ppm at Rainbow field [3]; up to 0.5 and 0.27 wt % Co and Ni in single EMPA analyses from Ashadze-1 field [63];

- Felsic-related fields (ppm, average Co and Ni contents, respectively): 114 and 16.0 at Hine Hina field; 210 and 2.42 in sulfides from Brothers Volcano [9]).

The bulk Co and Ni contents of ultramafic-related massive sulfides are typically higher than those of mafic-related mineralization, thus, Co and Ni (as well as their minerals) are considered the markers of ultramafic-associated mineralization [64–69]. However, a number of factors affect the distribution of Co and Ni, e.g., temperature, S fugacity, metal contents in the fluid, etc., thus, the absolute Co and Ni contents (and even Co/Ni ratio) of minerals can be independent from the type of substrate.

The Co/Ni ratio of pyrite from the Rainbow hydrothermal field was recognized as indicative of mafic- and ultramafic-dominated (seafloor and subseafloor, respectively) origin of sulfides: Co/Ni ratio of >1 and <1, respectively [66]. In our case, the Co/Ni ratio of pyrite is >>1 (av. 30), which is in line with its seafloor origin. Seafloor pyrite does frequently exhibit the Co/Ni ratio of >1 irrespectively of the type of substrate (mafic or ultramafic) [9]. Even selected analyses of pyrite from felsic-dominated environments either have "ultramafic-dominated" Co/Ni ratios of ~1 or <1 (e.g., Jade field or Volcano 19) or maximum Co and Ni contents, which exceed those typical of ultramafic rocks (e.g., 488 and 4552 ppm Ni and Co, respectively) [9]. All this indicates that this ratio is caused by more complex reasons, and the host rock influence is the least reasonable explanation, as was recently suggested on the basis of rPCA analysis of bulk composition of seafloor massive sulfides [70].

We believe that, at least, the temperature control is first responsible for the Co and Ni contents and Co/Ni ratio of pyrite. For example, the Co/Ni ratio of seafloor pyrite from Fe-rich massive sulfides of the basalt-associated Wocan hydrothermal field (Carlsberg Ridge) varies from 13 in early higher-T pyrite-1 to 0.02 and 0.21 in lower-T pyrite-2 and -3, respectively (Co/Ni ratios are calculated on the basis of average contents from Table 3 in [17]). The similar low Co/Ni ratio (0.02) is typical of low-T colloform pyrite from black (gray) smokers of the Paleozoic Yaman-Kasy volcanic-hosted massive sulfide deposit (South Urals) [2] or Suiyo Volcano, PACMANUS area and Axial Seamount [3].

Relatively moderate Co and low Ni contents of the Ashadze-2 late crystalline pyrite suggest that it was deposited from moderate- to low-temperature fluid, because the Co contents in hydrothermal fluids decreases below 350 °C [36]. Relatively low temperatures of formation of pyrite are also indicated by much higher (in comparison with isocubanite, chalcopyrite, and bornite; Table S1) contents of V, which is considered a seawater-derived element [15].

5.2.2. Isocubanite

Isocubanite of the Ashadze-2 hydrothermal field is a major carrier of Co, and the level of its Co contents is similar to that of isocubanite from ultramafic-associated Ashadze-1 (0.61 wt % [63]) and Rainbow (0.02–0.52 wt % [66] and 0.41–0.73 wt % [71]) hydrothermal fields. Nickel in isocubanite from these hydrothermal fields exhibitsg both negligible contents (<<1 ppm) (Ashadze-2 field), EMPA-undetectable contents (Ashadze-1, Rainbow fields) or relatively high contents up to 0.52 (Ashadze-1 field) and 0.32–0.39 wt % (Rainbow field) [24,63,66,71]. In one sample from the Rainbow field, seafloor isocubanite is Co-free, but is Ni-bearing (0.55–0.80 wt %) [71].

The low Ni contents of the Ashadze-2 isocubanite, first of all, reflect the low Ni contents in the hydrothermal fluid. Example of the Rainbow hydrothermal field [66] shows that the Co/Ni ratio of Cu–Fe sulfides (both isocubanite and chalcopyrite) has no direct correlation with host rock units. The Co/Ni ratio of the Rainbow isocubanite from stockwork samples and smoker chimneys is <1 and >1, respectively, which is in agreement with their subseafloor and seafloor origin, respectively. However, isocubanite from selected subseafloor samples exhibit high Co/Ni ratio (1–52), which, in the pyrite case, is typical of seafloor samples, and vice versa, according to the data of [71], some seafloor isocubanite contains Ni instead of Co indicating Co/Ni ratio of <<1.

Isocubanite is one of the high-T (~350 °C) minerals to precipitate in seafloor conditions [39,72]. In our case, a number of reasons (or their combinations) can be responsible for the low Ni contents of high-T isocubanite. First, ultramafic environment is considered to provide highly reducing conditions [73], which are more efficient for extraction and transportion of Co [69]. This is true, at least for seafloor conditions, because the bulk analyses of massive sulfides from the Rainbow and Logatchev hydrothermal fields exhibit high Co and low Ni contens in seafloor massive sulfides [65,67], and vice versa in subseafloor sulfide-bearing samples [67].

It was concluded as a result of experimental works that Ni in aqueous hydrothermal fluids showed a pronounced dependence on the chlorinity of the fluid [74], i.e., the Ni contents increase with increasing salinity of the fluids. In MAR ultramafic-related hydrothermal fields, the highest Ni contents are detected in seafloor sulfides from the Rainbow hydrothermal field, the fluid of which has one of the most phase separated Cl-rich compositions (750 mM Cl) [73]. Evidence of phase separation was also registered at the Ashadze-1 and Ashazde-2 fields in 2007 [75]. A 2007-fluid at the Ashadze-2 field had Cl content of 326 mM (~1.92 wt % NaCl), which is 1.65 times lower than the salinity of seawater (540 mM) [76]. All these data could indicate that Ni-poor isocubanite from our samples crystallized from less saline fluids, which dissolve low amount of Ni.

5.2.3. Chalcopyrite

Chalcopyrite (as well as isocubanite) from the Ashadze-2 hydrothermal field is remarkable for high Se (av. 1166 ppm) and relatively high Te (av. 71.55 ppm) contents. Similar (within standard deviation) Se and Te contents are detected in chalcopyrite from black smokers of the Rainbow (934 and 68 ppm, respectively) and Broken Spur (1983 and 92 ppm, respectively) hydrothermal fields [3]. Similar (within standard deviation) Se-rich but Te-poor chalcopyrite is recorded in black and gray smokers of the Logatchev (1035 and 38 ppm, respectively), EPR 9°11′ N (1184 and 26, respectively), Lucky Strike (928 and 0.4 ppm, respectively), Galapagos Ridge (857 and 0.14 ppm, respectively), Menez Gwen (1517 and 0.5 ppm, respectively), and Axial Seamount (1258 and 1.3 ppm, respectively) [3]. Chalcopyrite from clear and white smokers is typically strongly depleted in both TEs (<<10 ppm) [3].

The elevated Se and Te contents in chalcopyrite are expected in high-T conditions, which are favorable for substitution of Se and Te for S [2,3,8,9,40,77]. Approximate temperature can be deduced from the results of experiments of [78], which demonstrated that chalcopyrite can dissolve at least 0.5 mol % eskebornite ($CuFeSe_2$) at 390 °C, which corresponds to ~2150 ppm Se. The highest Se contents of the Ashadze-2 chalcopyrite attain 2964 ppm and we can suspect that temperature of the fluid could have reached more than 390 °C, at least during the formation of Se-rich chalcopyrite grains. The high

formation temperature of chalcopyrite is also indirectly supported higher (relative to isocubanite) Ni contents, since Ni could have been more mobile at temperatures of >400 °C [69].

5.2.4. Bornite

Bornite is a common secondary mineral in seafloor hydrothermal fields, which replaces primary sulfides as a result of waning hydrothermal activity and influence of seawater [17,18,63,65,79–81]. Primary high-T bornite is reported from Cu-rich chimneys of the Snake Pit hydrothermal field [82] and several black smokers from the TAG hydrothermal field, where bornite is associated with chalcopyrite and pyrite [83]. In both cases, the presence of bornite is indicative of more oxidizing conditions.

In the Ashadze-2 samples, bornite replaces chalcopyrite and sphalerite pointing to its secondary origin, but its enrichment in a suite of "high-T" TEs (Co, Se, In, Sn, Te) relative to chalcopyrite is rather atypical of a lower-T Cu–Fe sulfide. The contents of seawater-derived U and V in Ashadze-2 bornite are even lower in comparison with chalcopyrite. In contrast, secondary bornite, e.g., from the Wocan hydrothermal field is extremely enriched in U in comparison with chalcopyrite, whereas primary bornite is enriched in Sn and In relative to secondary bornite [17].

Very few data on TE composition of seafloor bornite are available now and the comparison is strongly limited. Nonetheless, it is evident that the Ashadze-2 bornite is extremely enriched in Se (av. 1409 ppm) comparing to bornite from the MESO (200 ppm Se), Wocan (av. 1 ppm Se) and Kairei (av. 372 ppm Se) hydrothermal fields [17,18,80]. On continents, a primary high-Se bornite was found in high-T Moberg and Glava Cu–Ag–(Au)–Mo vein-type granite-associated deposits in the Late Proterozoic Sveconorwegian province (1156 and 4617 ppm Se in Moberg bornite, and 2224 ppm Se in Glava bornite) and Ocna de Fier Fe–Cu–(Zn–Pb) skarn deposit in Romania (1046 ppm Se) [5]. The main difference between Ashazde-2 bornite and continental ones is the Co enrichment of seafloor bornite and the Ag and Bi enrichment of continental bornite.

Similarly to chalcopyrite, we can suggest that the incorporation of Co, Se, and Sn into the crystal lattice of bornite is also favored by high-T conditions. This conclusion means strong temperature fluctuations during the formation of massive sulfide with chalcopyrite, sphalerite and pyrite/bornite.

5.2.5. Isocubanite + Chalcopyrite Mixture

This subseafloor mineral assemblage in altered gabbro is remarkable for its enrichment in several TEs: Ni (which is typical of ultramafic rocks [69]) and Zn, As, Mo, Cd, Sb, Tl, and Pb (a suite of TEs more typical of mafic or even felsic volcanic rocks [82,84]). In mineralogy, this sample resembles stringer-disseminated mineralization in serpentinites and basalts of the Rainbow [66] and Snake Pit [82] hydrothermal fields, respectively. The Rainbow minerals demonstrate similar Zn contents (0.66 wt % in isocubanite), but lower Ni (0.26 and 0.13 wt % in isocubanite and chalcopyrite, respectively) and Co (0.09 and 0.03 wt % in isocubanite and chalcopyrite, respectively) contents. The Zn-rich Cu–Fe sulfides are reported from subseafloor samples of the Snake Pit hydrothermal field [85]. In subseafloor Cu–Fe minerals both of the Ashazde-2 and Rainbow fields, the Co/Ni ratio is <1, indicating that this ratio is more sensitive for the subseafloor mineralization, because Ni is directly extracted from silicates or magmatic sulfides and is more effectively incorporated into subseafloor Cu–Fe sulfides [70].

As indicated in Section 5.1.6, the erratic Ni contents and positive correlation between Ni and As and Sb most likely indicate the presence of a sulfarsenide inclusions, in particular, Sb-bearing gersdorffite. This is a typical mineral of many continental ultramafic-related sulfide deposits, which are considered possible fossil analogs of the present-day ultramafic-associated hydrothermal fields [69]: Eastern Metals, Canada [86], Limassol Forest area in Troodos Ophiolites, Cyprus [87,88], Bou-Azzer deposit in Morocco [89], Outokumpu deposit in Finland [90], Ivanovka deposit in the South Urals [91]. Abundant accessory arsenide mineralization is also typical of the Ishkinino and Dergamysh Co-bearing massive sulfide deposits associated with ultramafic rocks of the Main Uralian Fault, South Urals [92]. In the Ishkinino deposits, gersdorffite contains up to 0.79 wt % Sb [93].

The low (relative to seafloor Cu–Fe sulfides) Se contents and higher contents of Zn, Cd, Tl, and Pb of isocubanite + chalcopyrite mixture indicate that (i) the temperature of the formation of this assemblage could have been lower in comparison with its seafloor counterparts; and (ii) they were probably sourced from the mafic domains of the hydrothermal field.

5.3. Behavior of Gold in Ashadze-2 Sulfides

Gold in the studied samples of the Ashadze-2 hydrothermal field is present in visible and invisible forms. The SEM-visible form includes very small grains in chalcopyrite and covellite and the isocubanite–covellite boundary. It was previously considered that gold in seafloor sulfide systems mostly tend to the lower-T assemblages with sphalerite, barite or amorphous silica and its association with Cu is mainly due to supergene reworking [60,94–96]. Further works revealed that native gold can also be found in assemblage with primary Cu sulfides indicating that, under certain conditions, high-T hydrothermal fluids can be saturated with respect to native gold [81,97–99].

The assemblage of native gold and Cu–Fe minerals in samples from stations 233 and 240 of the Ashadze-2 hydrothermal field, from one hand, is similar to copper–gold association of Cu-rich chimneys of the Logatchev hydrothermal field [97]. The difference lies in Ag content: no more than 2 wt % for the Logatchev gold and 7.35 wt % for the Ashadze-2 gold. We can suggest that the Ashadze-2 chalcopyrite-hosted native gold precipitated under decreasing temperature after the formation of chalcopyrite but before the crystallization of sphalerite, which overgrows chalcopyrite. The lower Ag contents of native gold, which was found in covellite and at the isocubanite–covellite boundary, are in line with its possible secondary origin resulted from reworking of the earlier hydrothermal more argentiferous gold [94,97].

The invisible form of occurrence of Au is supported by LA-ICP-MS analysis of sulfides. The lowest Au contents are detected in pyrite, isocubanite and subseafloor isocubanite + chalcopyrite mixture. Secondary covellite is enriched in Au relative to primary sulfides. Covellite-A, chalcopyrite, and bornite with similar Au contents are the richest minerals with respect to gold (av. 6.23, 8.18, and 6.23 ppm Au, respectively). The erratic Au contents in chalcopyrite and bornite indicate that gold most likely occurs in the nano-sized gold particles. In covellite, the gold particles can have more complex occurrence being associated with phyllosilicates, which is evident from high correlation coefficients (see above). Correlation of Au with seawater-derived elements in covellite, bornite, and isocubanite + chalcopyrite mixture (see above) indicates the important role of seawater during its formation.

5.4. Role of Seawater in TE Redistribution in Sulfides

It was previously shown for the Semenov-2 hydrothermal field that covellite is enriched in most TEs relative to primary sulfides [11]. The Semenov-2 covellite replaces Zn (würtzite and sphalerite) and Cu–Fe (isocubanite and chalcopyrite) sulfides. Both covellite types are enriched in those TEs, which are present in primary minerals in form of mineral inclusions, and are depleted in TEs isomorphic for primary minerals.

Covellite from the Ashadze-2 hydrothermal field behaves similarly (Figure 8). Both covellite types are enriched in most TEs relative to primary sulfides. The enrichment in U, V, Mo, W, and, partly, As, supports the involvement of seawater during the formation of covellite.

Both covellites are depleted in Co, which substitutes for Fe in primary sulfides (Figure 8). The Ni contents are low in both primary sulfides and covellite-A and -B. Covellite-A is also depleted in As, which is isomorphic TE of pyrite. Other TEs in pyrite most likely reside as inclusions of other sulfides (sphalerite, chalcopyrite, galena), native gold, barite, or silicates (see Section 5.1.1), which can be dissolved by heated seawater during the replacement processes and formation of covellite.

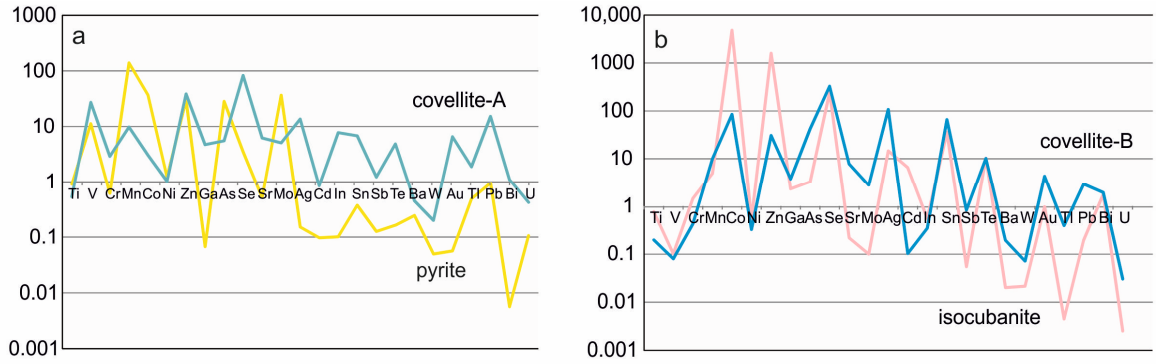

Figure 8. Comparative diagrams for the median trace element (TE) composition of pyrite and covellite-A (**a**) and isocubanite and covellite-B (**b**) (ppm).

In covellite-B, Co, Zn, Ga, Cd, In, and Te, which are referred to as isomorphic TEs in isocubanite, are also removed from the system, whereas Se, Ag, and Sn (isomorphic TEs of isocubanite as well) exhibit higher contents in covellite-B. The enrichment in Se, Ag, and Sn of covellite-B can probably indicate the dual mode of occurrence of these TEs: isomorphic and inclusion-related (e.g., clausthalite, native gold or stannite). The latter, for example, is a typical mineral of the MAR ultramafic-hosted hydrothermal fields [100].

The thermodynamic modeling shows that the mineral assemblages, which form as a result of MS/SW interaction and further conductive cooling of the solution, mainly depend on temperature, the presence of open porosity, and MS/SW ratio. In case of low MS/SW ratios and local equilibrium, accessory and rare minerals (e.g., native gold and galena) would be dissolved being further incorporated in newly formed minerals (e.g., covellite).

6. Conclusions

Trace element composition of sulfides from Cu-rich massive sulfide samples of the Ashadze-2 hydrothermal field is a result of influence of several important factors: local formation conditions, seawater entrapment, and host rocks. For local formation conditions, in particular, temperature plays a key role in the enrichment of primary sulfides in some trace elements. The high-T isocubanite from seafloor massive sulfides is strongly enriched in Co and, locally, in Se and the temperature of its deposition could have reached more than 350 °C. Secondary bornite, which replaces chalcopyrite, is also enriched in Se indicating its possible high-T formation conditions as well. Pyrite, which crystallized from moderate- low-T fluids, is depleted in many trace elements, including Co and Ni.

Covellite, which replaces sulfides, is generally enriched in trace elements relative to primary minerals, which reside in primary sulfides in form of mineral inclusions (e.g., native gold, galena, clausthalite) and is depleted in most isomorphic TEs of primary sulfides. Covellite is always rich in seawater-derived elements (U, V, Mo, W, and, locally, As) indicating the important role of seawater in its formation. Some trace element correlations advocate that, under certain conditions, metals can partition to gangue minerals as well. It is suggested that covellite shares some toxic (Pb, Cd, Tl, Ni) and precious (Au) trace elements with closely associated phyllosilicates. Subseafloor Cu–Fe sulfides in strongly altered gabbro are surprisingly enriched in Zn, Pb, Cd, and Tl, which could have been sourced from the mafic domains of the hydrothermal field.

Gold enriches all Cu–Fe and Cu sulfides, and occurs as finest and mostly nano-sized particles. The assemblage and composition of native gold probably indicate the presence of two generations: primary Ag-bearing gold associated with chalcopyrite and bornite and supergene purified gold associated with covellite (and possibly with phyllosilicates). The thermodynamic modeling supports an idea of the dissolution of accessory minerals (e.g., native gold and galena), which are affected by heated seawater, and the presence of metals (Au, Pb) in solution during the precipitation of covellite.

Although Co and Ni are traditionally considered the markers of ultramafic-related seafloor mineralization, the behavior of these metals much more strongly depends on the local formation conditions and morphological types of sulfides. In spite of the ultramafic environment, Ni in Ashadze-2 seafloor sulfides exhibits low to moderate contents and significantly enriches the subseafloor Cu–Fe sulfide aggregates. The use of the Co/Ni ratio for discriminating mafic- and ultramafic-associated sulfides often yields controversial results and, thus, is not warranted.

Supplementary Materials: The following are available online at http://www.mdpi.com/2075-163X/10/9/743/s1, Table S1: Chemical composition of sulfides from the Ashadze-2 hydrothermal field according to LA-ICP-MS analysis (ppm) and correlation matrices for elements.

Author Contributions: I.M., study of massive sulfides, interpretation of the results, writing and editing of paper; V.M., LA-ICP-MS analysis, interpretation of the results and editing of paper; G.T., physico-chemical modeling, interpretation of the results and editing of paper; S.M., processing of LA-ICP-MS analyses; L.D. and R.L., LA-ICP-MS analysis of sulfides; V.B. sampling and mapping of the hydrothermal field; V.K., electron microscopic studies; P.K., XRD analysis of samples and its interpretation. All authors have read and agreed to the published version of the manuscript.

Funding: This research was funded by State Contract of the IMin no. AAAA-A19-119061790049-3.

Acknowledgments: I.M. thanks staff of the Polar Marine Geosurvey Expedition (St-Petersburg, Russia) for the possibility of participation in the 30th cruise of R/V Professor Logatchev and massive sulfide sampling and G.A. Cherkashev for providing additional geological data. The authors thank two anonymous reviewers for their useful comments, which helped us to improve the paper.

Conflicts of Interest: The authors declare no conflict of interest.

References

1. Large, R.R.; Danyushevsky, L.; Hollit, H.; Maslennikov, V.V.; Meffre, S.; Gilbert, S.; Bull, S.; Scott, R.; Emsbo, P.; Thomas, H.; et al. Gold and trace element zonation in pyrite using a laser imaging technique: Implications for the timing of gold in orogenic and Carlin-style sediment-hosted deposits. *Econ. Geol.* **2009**, *104*, 635–668. [CrossRef]
2. Maslennikov, V.V.; Maslennikova, S.P.; Large, R.R.; Danyushevsky, L.V. Study of trace element zonation in vent chimneys from the Silurian Yaman-Kasy volcanic-hosted massive sulfide deposit (Southern Urals, Russia) using laser ablation-inductively coupled plasma mass spectrometry (LA-ICP-MS). *Econ. Geol.* **2009**, *104*, 1111–1141. [CrossRef]
3. Maslennikov, V.V.; Maslennikova, S.P.; Large, R.; Danyushevsky, L.; Herrington, R.J.; Ayupova, N.R.; Zaykov, V.V.; Lein, A.Y.; Tseluyko, A.S.; Melekestseva, I.Y.; et al. Chimneys in Paleozoic massive sulfide mounds of the Urals VMS deposits: Mineral and trace element comparison with modern black, grey, white and clear smokers. *Ore Geol. Rev.* **2017**, *85*, 64–106. [CrossRef]
4. Cook, N.J.; Ciobanu, C.L.; Pring, A.; Skinner, W.; Shimizu, M.; Danyushevsky, L.; Saini-Eidukat, B.; Melcher, F. Trace and minor elements in sphalerite: A LA-ICPMS study. *Geochim. Cosmochim. Acta* **2009**, *73*, 4761–4791. [CrossRef]
5. Cook, N.J.; Ciobanu, C.L.; Danyushevsky, L.; Gilbert, S. Minor and trace elements in bornite and associated Cu–(Fe)-sulfides: A LA-ICP-MS study. *Geochim. Cosmochim. Acta* **2011**, *75*, 6473–6496. [CrossRef]
6. Cook, N.J.; Ciobanu, C.L.; Williams, T. The mineralogy and mineral chemistry of indium in sulphide deposits and implications for mineral processing. *Hydrometallurgy* **2011**, *108*, 226–228. [CrossRef]
7. George, L.; Cook, N.J.; Ciobanu, C.L.; Wade, B.P. Trace and minor elements in galena: A reconnaissance LA-ICP-MS study. *Amer. Mineral.* **2015**, *100*, 548–569. [CrossRef]
8. Wohlgemuth-Ueberwasser, C.C.; Viljonen, F.; Petersen, S.; Vrster, C. Distribution and solubility limits of trace elements in hydrothermal black smoker sulfides: An in-situ LA-ICP-MS study. *Geochim. Cosmochim. Acta* **2015**, *159*, 16–41. [CrossRef]
9. Keith, M.; Häckel, F.; Haase, K.M.; Schwarz-Schampera, U.; Klemd, R. Trace element systematics of pyrite from submarine hydrothermal vents. *Ore Geol. Rev.* **2016**, *72*, 728–745. [CrossRef]
10. Reich, M.; Román, N.; Barra, F.; Morata, D. Silver-rich chalcopyrite from the active Cerro Pabellón geothermal system, Northern Chile. *Minerals* **2020**, *10*, 113. [CrossRef]

11. Melekestseva, I.Y.; Tret'yakov, G.A.; Nimis, P.; Yuminov, A.M.; Maslennikov, V.V.; Maslennikova, S.P.; Kotlyarov, V.A.; Beltenev, V.E.; Danyushevsky, L.V.; Large, R. Barite-rich massive sulfides from the Semenov-1 hydrothermal field (Mid-Atlantic Ridge, 13°30.87′ N): Evidence for phase separation and magmatic input. *Mar. Geol.* **2014**, *349*, 37–54. [CrossRef]
12. Melekestseva, I.Y.; Maslennikov, V.V.; Maslennikova, S.P.; Danyushevsky, L.; Large, R. Covellite from Semenov-2 hydrothermal field (13°31.13′ N, Mid-Atlantic Ridge): Enrichment in trace elements according to LA-ICP-MS analysis. *Dokl. Earth Sci.* **2017**, *473*, 291–295. [CrossRef]
13. Melekestseva, I.Y.; Maslennikov, V.V.; Tret'yakov, G.A.; Nimis, P.; Beltenev, V.E.; Rozhdestvenskaya, I.I.; Maslennikova, S.P.; Belogub, E.V.; Danyushevsky, L.; Large, R.; et al. Gold- and silver-rich massive sulfides from the Semenov-2 hydrothermal field, 13°31.13′ N, Mid-Atlantic Ridge: A case of magmatic contribution? *Econ. Geol.* **2017**, *112*, 741–773. [CrossRef]
14. Melekestseva, I.Y.; Maslennikov, V.V.; Safina, N.P.; Nimis, P.; Maslennikova, S.P.; Beltenev, V.; Rozhdestvenskaya, I.; Danyushevsky, L.; Large, R.; Artemyev, D.A.; et al. Sulfide breccias from the Semenov-3 hydrothermal field, Mid-Atlantic Ridge: Authigenic mineral formation and trace element pattern. *Minerals* **2018**, *8*, 321. [CrossRef]
15. Butler, I.B.; Nesbitt, R.V. Trace element distribution in the chalcopyrite wall of a black smoker chimney: Insights from laser ablation inductively coupled plasma mass spectrometry (LA-ICP-MS). *Earth Planet. Sci. Lett.* **1999**, *167*, 335–345. [CrossRef]
16. Wu, Z.; Sun, X.; Xu, H.; Konishi, H.; Wang, Y.; Wang, C.; Dai, Y.; Deng, X.; Yu, M. Occurrences and distribution of "invisible" precious metals in sulfide deposits from the Edmond hydrothermal field, Central Indian Ridge. *Ore Geol. Rev.* **2016**, *79*, 105–132. [CrossRef]
17. Wang, Y.; Han, X.; Petersen, S.; Frische, M.; Qiu, Z.; Li, H.; Wu, Z.; Cui, R. Mineralogy and trace element geochemistry of sulfide minerals from the Wocan hydrothermal field on the slow-spreading Carlsberg Ridge, Indian Ocean. *Ore Geol. Rev.* **2017**, *84*, 1–19. [CrossRef]
18. Wang, H.; Li, X.; Chu, F.; Li, Z.; Wang, J.; Yu, X.; Bi, D. Mineralogy, geochemistry, and Sr-Pb isotopic geochemistry of hydrothermal massive sulfides from the 15.2°S hydrothermal field, Mid-Atlantic Ridge. *J. Mar. Syst.* **2018**, *180*, 220–227. [CrossRef]
19. Beltenev, V.; Nescheretov, A.; Shilov, V.; Ivanov, V.; Shagin, A.; Stepanova, T.; Cherkashev, G.; Batuev, B.; Samovarov, M.; Rozhdestvenskaya, I.; et al. New discoveries at 12°58′ N and 44°52′ W, MAR: Initial results from the Professor Logatchev-22 cruise. *InterRidge News* **2003**, *12*, 13–14.
20. Beltenev, V.E.; Nescheretov, A.V.; Ivanov, V.N.; Shilov, V.; Rozhdestvenskaya, I.I.; Shagin, A.; Stepanova, T.V.; Andreeva, I.A.; Semenov, Y.P.; Sergeev, M.B.; et al. A new hydrothermal field in the axial zone of the Mid-Atlantic Ridge. *Dokl. Earth Sci.* **2004**, *397*, 690–693. (In Russian)
21. Cherkashev, G.A.; Ivanov, V.N.; Bel'tenev, V.I.; Lazareva, L.I.; Rozhdestvenskaya, I.I.; Samovarov, M.L.; Poroshina, I.M.; Sergeev, M.B.; Stepanova, T.V.; Dobretsova, I.G.; et al. Massive sulfide ores of the northern equatorial Mid-Atlantic Ridge. *Oceanology* **2013**, *53*, 607–619. [CrossRef]
22. Fouquet, Y.; Cherkashev, G.; Charlou, J.L.; Ondréas, H.; Birot, D.; Cannat, M.; Bortnikov, N.; Silantyev, S.; Sudarikov, S.; Cambon-Bonavita, M.A.; et al. Serpentine cruise ultramafic hosted hydrothermal deposits on the Mid-Atlantic Ridge: First submersible studies on Ashadze 1 and 2, Logatchev 2 and Krasnov vent fields. *InterRidge News* **2008**, *17*, 15–19.
23. Ondréas, H.; Cannat, M.; Fouquet, Y.; Normand, A. Geological context and vents morphology of the ultramafic-hosted Ashadze hydrothermal areas (Mid-Atlantic Ridge 13°N). *Geochem. Geophys. Geosys.* **2012**, *13*, Q0AG14. [CrossRef]
24. Firstova, A.; Stepanova, T.; Cherkashov, G.; Goncharov, A.; Babaeva, S. Composition and formation of gabbro-peridotite hosted seafloor massive sulfide deposits from the Ashadze-1 hydrothermal field, Mid-Atlantic Ridge. *Minerals* **2016**, *6*, 19. [CrossRef]
25. Cherkashev, G.A.; Stepanova, T.V.; Andreev, S.I.; Firstova, A.V.; Egorov, I.V.; Bel'tenev, V.I.; Ivanov, V.N.; Samovarov, M.L.; Rozhdestvenskaya, I.I.; Lazareva, L.I.; et al. Ore objects within Russian application area in the Northern equatorial part of the Mid-Atlantic Ridge. In *World Ocean. Vol. III. Solid Mineral Deposits and Gas Hydrates in the Ocean*; Lobkovsky, L.I., Cherkashev, G.A., Eds.; Nauchny Mir: Moscow, Russia, 2018; pp. 90–122. (In Russian)

26. Ayupova, N.R.; Melekestseva, I.Y.; Maslennikov, V.V.; Tseluyko, A.S.; Blinov, I.A.; Beltenev, V.E. Uranium accumulation in modern and ancient Fe-oxide sediments: Examples from the Ashadze-2 hydrothermal sulfide field (Mid-Atlantic Ridge) and Yubileynoe massive sulfide deposit (South Urals, Russia). *Sediment. Geol.* **2018**, *367*, 164–174. [CrossRef]
27. Danyushevsky, L.V.; Robinson, R.; Gilbert, S.; Norman, M.; Large, R.; McGoldrick, P.; Shelley, J.M.G. Routine quantitative multielement analysis of sulfide minerals by laser ablation ICP-MS: Standard development and consideration of matrix effects. *Geochem. Explor. Environ. Anal.* **2011**, *11*, 51–60. [CrossRef]
28. Longerich, H.P.; Jackson, S.E.; Gunte, D. Laser ablation inductively coupled plasma mass spectrometric transient signal data acquisition and analyte concentration calculation. *J. Anal. At. Spectrom.* **1996**, *11*, 899–904. [CrossRef]
29. Smirnov, V.I. *Correlation Methods in Paragenetic Analysis*; Nedra: Moscow, Russia, 1981; 174p. (In Russian)
30. Whitney, D.L.; Evans, B.W. Abbreviations for names of rock-forming minerals. *Am. Mineral.* **2010**, *95*, 185–187. [CrossRef]
31. Barton, P.B., Jr. Some ore textures involving sphalerite from the Furutobe mine, Akita Prefecture. *Jpn. Min. Geol.* **1978**, *28*, 293–300. [CrossRef]
32. Karpov, I.K.; Chudnenko, K.V.; Kulik, D.A. Modeling chemical mass transfer in geochemical processes: Thermodynamic relations, conditions of equilibrium, and numerical algorithms. *Am. J. Sci.* **1997**, *297*, 767–806. [CrossRef]
33. Steele, J.H.; Thorpe, S.A.; Turekian, K.K. (Eds.) *Marine Chemistry and Geochemistry: A Derivative of Encyclopedia of Ocean Sciences*, 2nd ed.; Elsiever: London, UK, 2010; 631p.
34. Tivey, M.K. Modeling chimney growth and associated fluid flow at seafloor hydrothermal vent sites. In *Seafloor Hydrothermal Systems: Physical, Chemical, Biological, and Geological Interactions*; Geophysical Monograph 91; Wiley: Hoboken, NJ, USA, 1995; pp. 158–173.
35. Koschinsky, A.; Garbe-Schönberg, D.; Sander, S.; Schmidt, K.; Gennerich, H.-H.; Strauss, H. Hydrothermal venting at pressure-temperature conditions above the critical point of seawater, 5°S on the Mid-Atlantic Ridge. *Geology* **2008**, *36*, 615–618. [CrossRef]
36. Metz, S.; Trefry, J.H. Chemical and mineralogical influences on concentrations of trace metals in hydrothermal fluids. *Geochim. Cosmochim. Acta* **2000**, *64*, 2267–2279. [CrossRef]
37. Tivey, M.K.; McDuff, R.E. Mineral precipitation in the walls of black smoker chimneys: A quantitative model of transport and chemical reaction. *J. Geophys. Res.* **1990**, *95*, 12617–12637. [CrossRef]
38. Chudnenko, K.V. *Thermodynamic Modeling in Geochemistry: Theory, Algorithms, Software, and Applications*; Geo: Novosibirsk, Russia, 2010; 287p. (In Russian)
39. Hannington, M.D.; Jonasson, I.R.; Herzig, P.M.; Petersen, S. Physical and chemical processes of seafloor mineralization at mid-ocean ridges. In *Seafloor Hydrothermal Processes*; Humphris, S.E., Zierenberg, R.A., Mullineaux, L.S., Thomson, R.E., Eds.; Geophysical Monograph 91; Wiley: Hoboken, NJ, USA, 1995; pp. 115–157.
40. Huston, D.L.; Sie, S.H.; Suter, G.F.; Cooke, D.R.; Both, R.A.Q. Trace elements in sulfide minerals from eastern Australian volcanic hosted massive sulfide deposits. Part I. Proton microprobe analyses of pyrite, chalcopyrite, and sphalerite. Part II. Selenium levels in pyrite comparison with $\delta^{34}S$ values and implication for the source of sulfur in volcanogenic hydrothermal systems. *Econ. Geol.* **1995**, *90*, 1167–1196. [CrossRef]
41. Deditius, A.P.; Utsunomiya, S.; Reich, M.; Kesler, S.E.; Ewing, R.C.; Hough, R.; Walshe, J. Trace metal nanoparticles in pyrite. *Ore Geol. Rev.* **2011**, *42*, 32–46. [CrossRef]
42. D'Orazio, M.; Biagioni, C.; Dini, A.; Vezzoni, S. Thallium-rich pyrite ores from the Apuan Alps, Tuscany, Italy: Constraints for their origin and environmental concerns. *Miner Deposita* **2017**, *52*, 687–707. [CrossRef]
43. Brumsack, H.-J. Geochemistry of recent TOC-rich sediments from the Gulf of California and the Black Sea. *Geologische Rundschau* **1989**, *78*, 851–882. [CrossRef]
44. Mikhailik, P.E.; Mikhailik, E.V.; Blokhin, M.G.; Zarubina, N.V. Sources of gallium in ferromanganese crusts from the Sea of Japan. *Rus. Geol. Geophys.* **2015**, *56*, 1148–1153. [CrossRef]
45. Abraitis, P.K.; Pattrick, R.A.D.; Vaughan, D.J. Variations in the compositional, textural and electrical properties of natural pyrite: A review. *Int. J. Miner. Process.* **2004**, *74*, 41–59. [CrossRef]

46. Dekov, V.; Scholten, J.; Garbe-Schönberg, C.-D.; Botz, R.; Cuadros, J.; Schmidt, M.; Stoffers, P. Hydrothermal sediment alteration at a seafloor **vent field: Grimsey graben, Tj**örnes Fracture Zone, north of Iceland. *J. Geophys. Res.* **2008**, *113*, B11101. [CrossRef]
47. Brett, R.; Evans, H.T., Jr.; Gibson, E.K., Jr.; Hedenquist, J.Y.; Windless, M.-V.; Sommer, M.A. Mineralogical studies of sulfide samples and volatile concentrations of basalt glasses from the Southern Juan de Fuca Ridge. *J. Geophys. Res.* **1987**, *92*, 11373–11379. [CrossRef] [PubMed]
48. George, L.L.; Cook, N.J.; Ciobanu, C.L. Partitioning of trace elements in co-crystallized sphalerite–galena–chalcopyrite hydrothermal ores. *Ore Geol. Rev.* **2016**, *77*, 97–116. [CrossRef]
49. George, L.L.; Cook, N.J.; Browie, B.B.P.; Ciobanu, C.L. Trace elements in hydrothermal chalcopyrite. *Mineral. Mag.* **2018**, *82*, 59–88. [CrossRef]
50. Rybicka, E.H.; Calmano, W.; Breeger, A. Heavy metals sorption/desorption on competing clay minerals; an experimental study. *Appl. Clay Sci.* **1995**, *9*, 369–381. [CrossRef]
51. Zhao, X.; Qiang, S.; Wu, H.; Yang, Y.; Shao, D.; Fang, L.; Liang, J.; Li, P.; Fan, Q. Exploring the sorption mechanism of Ni(II) on illite: Batch sorption, modelling, EXAFS and extraction investigations. *Sci. Rep.* **2017**, *7*, 8495. [CrossRef]
52. Cao, C.-Y.; Liang, C.-H.; Yin, Y.; Du, L.-Y. Thermal activation of serpentine for adsorption of cadmium. *J. Hazard. Mater.* **2017**, *329*, 222–229. [CrossRef]
53. Martin, L.A.; Wissocq, A.; Benedetti, M.F.; Latrille, C. Thallium (Tl) sorption onto illite and smectite: Implications for Tl mobility in the environment. *Geochim. Cosmochim. Acta* **2018**, *230*, 1–16. [CrossRef]
54. Donat, R. The removal of uranium (VI) from aqueous solutions onto natural sepiolite. *J. Chem. Thermodynam.* **2009**, *41*, 829–835. [CrossRef]
55. Sun, Y.; Li, J.; Wang, X. The retention of uranium and europium onto sepiolite investigated by macroscopic, spectroscopic and modelling techniques. *Vol. Geochim. Cosmochim. Acta* **2009**, *140*, 621–643. [CrossRef]
56. Hein, J.R.; Mizell, K.; Koschinsky, A.; Conrad, T. Deep-ocean mineral deposits as a source of critical metals for high- and green-technology applications: Comparison with land-based deposits. *Ore Geol. Rev.* **2013**, *51*, 1–14. [CrossRef]
57. Hein, J.R.; Spinardi, F.; Okamoto, N.; Mizell, K.; Thorburn, D.; Tawake, A. Critical metals in manganese nodules from the Cook Islands EEZ, abundances and distributions. *Ore Geol. Rev.* **2015**, *68*, 97–116. [CrossRef]
58. Hein, J.R.; Koschinsky, A. Deep-ocean ferromanganese crusts and nodules. In *Treatise on Geochemistry*, 2nd ed.; Holland, H.D., Turekian, K.K., Eds.; Elsevier: Amsterdam, The Netherlands, 2014. [CrossRef]
59. Bogdanov, Y.A.; Vikent'ev, I.V.; Lein, A.Y.; Bogdanova, O.Y.; Sagalevich, A.M.; Sivtsov, A.V. Low-temperature hydrothermal deposits in the rift zone of the Mid-Atlantic Ridge. *Geol. Ore Dep.* **2008**, *50*, 119–134. [CrossRef]
60. Hannington, M.; Herzig, P.; Scott, S.; Thompson, G.; Rona, P. Comparative mineralogy and geochemistry of gold-bearing sulfide deposits on the mid-ocean ridges. *Mar. Geol.* **1991**, *101*, 217–248. [CrossRef]
61. Belissont, R.; Munoz, M.; Boiron, M.-C.; Luais, B.; Mathon, O. Germanium crystal chemistry in Cu-bearing sulfides from micro-XRF mapping and micro-XANES spectroscopy. *Minerals* **2019**, *9*, 227. [CrossRef]
62. Firstova, A.; Stepanova, T.; Sukhanova, A.; Cherkashov, G.; Poroshina, I. Au and Te minerals in seafloor massive sulphides from Semyenov-2 hydrothermal field, Mid-Atlantic Ridge. *Minerals* **2019**, *9*, 294. [CrossRef]
63. Mozgova, N.N.; Trubkin, N.V.; Borodaev, Y.S.; Cherkashov, G.A.; Stepanova, T.V.; Semkova, T.A.; Uspenskaya, T.Y. Mineralogy of massive sulfides from the Ashadze hydrothermal field, 13°N, Mid-Atlantic Ridge. *Can. Miner.* **2008**, *46*, 545–567. [CrossRef]
64. Mozgova, N.N.; Krasnov, S.G.; Batuyev, B.N.; Borodaev, Y.S.; Efimov, A.V.; Markov, V.F.; Stepanova, T.V. The first report of cobalt pentlandite from a Mid-Atlantic Ridge hydrothermal deposit. *Can. Miner.* **1996**, *34*, 23–28.
65. Lein, A.Y.; Cherkashov, G.A.; Ul'yanov, A.A.; Ul'yanova, N.V.; Stepanova, T.V.; Sagalevich, A.M.; Bogdanov, Y.A.; Gurvich, E.G.; Torokhov, M.P. Mineralogy and geochemistry of sulfide ores from the Logachev-2 and Rainbow fields: Similar and distinctive features. *Geokhimiya* **2003**, *41*, 271–294. (In Russian)
66. Marques, A.F.A.; Barriga, F.J.A.S.; Chavagnac, V.; Fouquet, Y. Mineralogy, geochemistry, and Nd isotope composition of the Rainbow hydrothermal field, Mid-Atlantic Ridge. *Miner. Deposita* **2006**, *41*, 52–67. [CrossRef]
67. Marques, A.F.A.; Barriga, F.J.A.S.; Scott, S.D. Sulfide mineralization in an ultramafic-rock hosted seafloor hydrothermal system: From serpentinization to the formation of Cu–Zn–(Co)-rich massive sulfides. *Mar. Geol.* **2007**, *245*, 20–39. [CrossRef]

68. Borodaev, Y.S.; Bryzgalov, I.A.; Mozgova, N.N.; Uspenskaya, T.Y. Pentlandite and Co-enriched pentlandite as characteristic minerals of modern hydrothermal sulfide mounds hosted by serpentinized ultramafic rocks (Mid-Atlantic Ridge). *Moscow Univ. Geol. Bul.* **2007**, *62*, 85–97. [CrossRef]
69. Fouquet, Y.; Cambon, P.; Etoubleau, J.; Charlou, J.-L.; Ondréas, H.; Barriga, F.J.A.S.; Cherkashov, G.; Semkova, T.; Poroshina, I.; Bohn, M.; et al. Geodiversity of hydrothermal processes along the Mid-Atlantic Ridge and ultramafic-hosted mineralization: A new type of oceanic Cu-Zn-Co-Au volcanogenic massive sulfide deposits. In *Diversity of Hydrothermal Systems on Slow Spreading Ocean Ridges*; Rona, P.A., Devey, C.W., Dyment, J., Murton, B.J., Eds.; AGU Geophys. Monograph; Wiley: Hoboken, NJ, USA, 2010; pp. 321–368.
70. Toffolo, L.; Nimis, P.; Tret'yakov, G.A.; Melekestseva, I.Y.; Beltenev, V.E. Seafloor massive sulfides from mid-ocean ridges: Exploring the causes of their geochemical variability with multivariate analysis. *Earth-Sci. Rev.* **2020**, *201*, 102958. [CrossRef]
71. Bogdanov, Y.A.; Bortnikov, N.S.; Vikent'ev, I.V.; Lein, A.Y.; Gurvich, E.G.; Sagalevich, A.M.; Simonov, V.A.; Ikorskii, S.V.; Stavrova, O.O.; Apollonov, V.N. Mineralogical–geochemical peculiarities of hydrothermal sulfide ores and fluids in the Rainbow field associated with serpentinites, Mid-Atlantic Ridge (36°14′ N). *Geol. Rudn. Mestorozh.* **2002**, *44*, 444–473. (In Russian)
72. Scott, S.D. Chemical behaviour of sphalerite and arsenopyrite in hydrothermal and metamorphic environments. *Mineral. Mag.* **1983**, *47*, 427–435. [CrossRef]
73. Douville, E.; Charlou, J.L.; Oelkers, E.H.; Bienvenu, P.; Jove Colon, C.F.; Donval, J.P.; Fouquet, Y.; Prieur, D.; Appriou, P. The Rainbow vent fluids (36°14′ N, MAR): The influence of ultramafic rocks and phase separation on trace metal content in Mid-Atlantic Ridge hydrothermal fluids. *Chem. Geol.* **2002**, *184*, 37–48. [CrossRef]
74. Watenphul, A.; Scholten, L.; Beermann, O.; Kavner, A.; Alraun, P.; Falkenberg, G.; Newville, M.; Lanzirotti, A.; Schmidt, C. Cu and Ni solubility in high-temperature aqueous fluids. In Proceedings of the AGU 2013 Fall Meeting, San Francisco, CA, USA, 9–13 December 2013. abstract id MR33A-2311.
75. Charlou, J.L.; Donval, J.P.; Konn, C.; Ondréas, H.; Fouquet, Y. High production and fluxes of H_2 and CH_4 and evidence of abiotic hydrocarbon synthesis by serpentinization in ultramafic-hosted hydrothermal systems on the Mid-Atlantic Ridge. In *Diversity of Hydrothermal Systems on Slow Spreading Ocean Ridges*; Rona, P.A., Devey, C.W., Dyment, J., Murton, B.J., Eds.; AGU Geophys. Monograph; Wiley: Hoboken, NJ, USA, 2010; pp. 265–296.
76. Bischoff, J.L.; Rosenbauer, R.J. The critical point and two-phase boundary of seawater, 200–500 °C. *Earth Planet. Sci. Let.* **1984**, *68*, 172–180. [CrossRef]
77. Auclair, G.; Fouquet, Y.; Bohn, M. Distribution of selenium in high-temperature hydrothermal sulfide deposits at 13°N, East Pacific Rise. *Can. Mineral.* **1987**, *25*, 577–588.
78. Bethke, P.M.; Barton, P.B. Distribution of some minor elements between coexisting sulfide minerals. *Econ. Geol.* **1971**, *66*, 140–163. [CrossRef]
79. Butler, I.B.; Fallick, A.E.; Nesbitt, R.V. Mineralogy, sulphur isotope geochemistry and the development of sulphide structures at the Broken Spur hydrothermal vent site, 29°10'N, Mid-Atlantic Ridge. *J. Geol Soc.* **1998**, *155*, 773–785. [CrossRef]
80. Halbach, P.; Blum, N.; Münch, U.; Plüger, W.; Garbe-Schönberg, D.; Zimmer, M. Formation and decay of a modern massive sulfide deposit in the Indian Ocean. *Miner. Deposita* **1998**, *33*, 302–309. [CrossRef]
81. Berkenbosch, H.A.; de Ronde, C.E.J.; Gemmel, J.B.; McNeil, A.W.; Goemann, K. Mineralogy and formation of black smoker chimneys from Brothers submarine volcano, Kermadec Arc. *Econ. Geol.* **2012**, *107*, 1613–1633. [CrossRef]
82. Fouquet, Y.; Wafik, A.; Cambon, P.; Mevel, C.; Meyer, G.; Gente, P. Tectonic setting and mineralogical and geochemical zonation in the Snake Pit sulfide deposit (Mid-Atlantic Ridge at 23° N). *Econ. Geol.* **1993**, *88*, 2018–2036. [CrossRef]
83. Hannington, M.D.; Tivey, M.K.; Larocque, A.C.; Petersen, S.; Rona, P.A. The occurrence of gold in sulfide deposits on the TAG hydrothermal field, Mid-Atlantic Ridge. *Can. Miner.* **1995**, *33*, 1285–1310.
84. Petersen, S.; Herzig, P.M.; Schwarz-Schampera, U.; Hannington, M.D.; Jonasson, I.R. Hydrothermal precipitates associated with bimodal volcanism in the Central Bransfield Strait, Antarctica. *Miner. Deposita* **2004**, *39*, 358–379. [CrossRef]
85. Ocean Drilling Program Leg 106 Scientific Party. Drilling the Snake Pit hydrothermal sulfide deposit on the Mid-Atlantic Ridge at 23°22′ N. *Geology* **1986**, *14*, 1004–1007. [CrossRef]

86. Auclair, M.; Gauthier, M.; Trottier, J.; Jebrak, M.; Chartrand, F. Mineralogy, geochemistry and paragenesis of the Eastern Metals serpentinite-associated Ni-Cu-Zn Deposit, Quebec Appalachians. *Econ. Geol.* **1993**, *88*, 123–138. [CrossRef]
87. Foose, M.P.; Economou, M.; Panayiotou, A. Compositional and mineralogic constraints on the genesis of ophiolite hosted nickel mineralization in the Pevkos Area, Limassol Forest, Cyprus. *Mineral. Deposita* **1985**, *20*, 234–240. [CrossRef]
88. Thalhammer, O.; Stumpfl, E.F.; Panayiotou, A. Postmagmatic, hydrothermal origin of sulfide and arsenide mineralization at Limassol Forest, Cyprus. *Mineral. Deposita* **1986**, *21*, 95–105. [CrossRef]
89. Leblanc, M. Co-Ni arsenide deposits, with accessory gold, in ultramafic rocks from Morocco. *Can. J. Earth Sci.* **1986**, *23*, 1592–1602. [CrossRef]
90. Peltola, E. Origin of Precambrian copper sulfides of the Outokumpu district, Finland. *Econ. Geol.* **1978**, *73*, 461–477. [CrossRef]
91. Nimis, P.; Tesalina, S.G.; Omenetto, P.; Tartarotti, P.; Lerouge, C. Phyllosilicate minerals in the hydrothermal mafic–ultramafic-hosted massive-sulfide deposit of Ivanovka (southern Urals): Comparison with modern ocean seafloor analogues. *Contrib. Mineral. Petrol.* **2004**, *147*, 363–383. [CrossRef]
92. Melekestseva, I.Y.; Zaykov, V.V.; Nimis, P.; Tret'yakov, G.A.; Tesalina, S.G. Cu–(Ni–Co–Au)-bearing massive sulfide deposits associated with mafic–ultramafic rocks of the Main Urals Fault, South Urals: Geological structures, ore textural and mineralogical features, comparison with modern analogs. *Ore Geol. Rev.* **2013**, *52*, 18–36. [CrossRef]
93. Melekestseva, I.Y. *Heterogeneous Cobalt-bearing Massive Sulfide Deposits in Ultramafic Rocks from the Paleoisland–arc Structures*; Nauka: Moscow, Russia, 2007; 245p. (In Russian)
94. Hannington, M.D.; Thompson, G.; Rona, P.A.; Scott, S.D. Gold and native copper in supergene sulphides from the Mid-Atlantic Ridge. *Nature* **1988**, *333*, 64–66. [CrossRef]
95. Herzig, P.M.; Hannington, M.D.; Fouquet, Y.; von Stackelberg, U.; Petersen, S. Gold-rich polymetallic sulfides from the Lau back arc and implications for the geochemistry of gold in sea-floor hydrothermal systems of the Southwest Pacific. *Econ. Geol.* **1993**, *88*, 2182–2209. [CrossRef]
96. Petersen, S.; Kuhn, T.; Herzig, P.M.; Hannington, M.D. Factors controlling precious and base-metal enrichments at the ultramafic-hosted Logatchev hydrothermal field, 14°45'N on the MAR: New insights from cruise M60/3. In *Mineral Deposits Research: Meeting the Global Challenge*; Mao, J., Bierlein, F.P., Eds.; Springer: Berlin/Heidelberg, Germany, 2005; Chapter 6–21; pp. 679–983.
97. Murphy, P.J.; Meyer, G. A gold-copper association in ultramafic-hosted hydrothermal sulfides from the Mid-Atlantic Ridge. *Econ. Geol.* **1998**, *93*, 1076–1083. [CrossRef]
98. De Ronde, C.E.J.; Massoth, G.J.; Butterfield, D.A.; Christenson, B.W.; Ishibashi, J.; Ditchburn, R.G.; Hannington, M.D.; Brathwaite, R.L.; Lupton, J.E.; Kamenetsky, V.S.; et al. Submarine hydrothermal activity and gold-rich mineralization at Brothers Volcano, Kermadec Arc, New Zealand. *Miner. Deposita* **2011**, *46*, 541–584. [CrossRef]
99. Pokrovski, G.S.; Akinfiev, N.N.; Borisova, A.Y.; Zotov, A.V.; Kouzmanov, K. Gold speciation and transport in geological fluids: Insights from experiments and physical-chemical modeling. *Geol. Soc. Spec. Publ.* **2014**, *402*, 9–70. [CrossRef]
100. Evrard, C.; Fouquet, Y.; Moëlo, Y.; Rinnert, E.; Etoubleau, J.; Langlade, J.A. Tin concentration in hydrothermal sulphides related to ultramafic rocks along the Mid-Atlantic Ridge: A mineralogical study. *Eur. J. Mineral.* **2015**, *27*, 627–638. [CrossRef]